

國立臺灣大學理學院大氣科學研究所

碩士論文

Graduate Institute of Atmospheric Sciences

College of Science

National Taiwan University

Master Thesis

地形約束下之等熵座標平衡模式

Isentropic Model of Topographically Bound Balanced
Motions

彭達凱

Da-Kai Peng

指導老師：郭鴻基 博士

Advisor : Hung-Chi Kuo, Ph.D.

中華民國 110 年 01 月

January 2021

誌謝



一本論文的完成，背後有著許多人的幫助。感謝郭鴻基老師這兩年來的諄諄教誨，在這間研究室總是可以學到新的知識，老師豐富的學識總是讓我驚嘆，除了研究上不遺餘力地給予幫助，也教導了我們許多人生的道理。感謝動力模擬實驗室的每個人。美雲作為實驗室的大家長，總是協助我們處理各種大小事。虹叡作為實驗室的大前輩，不但給了我許多技術上及研究上的幫助，也給了我以過來人身分的各種經驗分享；徐驊是一起待在實驗室時間最長的夥伴，學術探討以及其他有趣的話題豐富了我的碩士生涯；品鈞不但是大學物理系的同學，也在研究上給了我許多的啟發，思考方式相近的我們總是能夠在研究上激盪出豐富的學術能量；亭佑在我快要被論文研究和大量瑣事壓的喘不過氣的時候，給予了很多及時的幫助。因為有你們這些實驗室的好夥伴們，我知道我在研究的路上不是一個人。感謝晏寧在論文寫作上細心的給予建議。感謝婉瑜、顥瑄，在這個短短的學期，身旁多了你們的歡笑聲。感謝大氣系的其他朋友們，在修課以及研究上提供的幫助。大氣系是一個溫暖的地方，讓身為異鄉人的我在此地仍然有家的感覺。

感謝命運中的一切安排，雖然不總是那麼完美，但成長路上的顛顛簸簸，都是茁壯成人的必經之路。拿到碩士學位，只是我實現夢想的第一步。期許未來的自己，能夠義無反顧的繼續前進，無論在學術目標上或是其他人生目標上，都能夠奮力的向前邁進，走出只屬於自己的、不後悔的道路。

彭達凱

2021.2.5 動力與模擬研究室 D&M Lab

摘要



位渦蘊含平衡大氣中之熱力及動力資訊。在靜力平衡近似和水平平衡關係下，從位渦場中可以得到平衡風場及溫度場，此種特性被稱為「位渦反演」。位渦反演涉及解橢圓形偏微分方程，其反演結果是非局部的。若我們有位渦場，則可以有效的反演出平衡動力以及熱力場。本研究探討地形約束下之等熵座標平衡運動，即等熵面與地形相交如何影響平衡流場。其中「無質量層」方法幫助我們求解等熵面與地形相交需要的數學技巧。

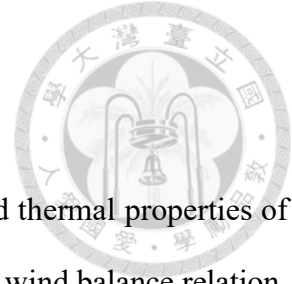
本研究主要參考 Silvers and Schubert (2012) 和 Fulton et al. (2017) 對於二維線性平衡模式的工作。我們延伸建立了等熵座標之二維線性平衡模型和三維線性與非線性平衡模式。利用這些模式，我們重現了 Silvers and Schubert (2012)對低層噴流的動力研究，在此之上並給予了地表加熱以及地形冷卻效應的量化分析，此外，我們也發現低層逆溫層在不同等熵座標高度下，根據逆溫層是否碰觸地形，分別有增強或削弱低層噴流的強度的效果。此外我們利用非線性平衡模式模擬類似於颱風結構的位渦場，並在中心上層設置負位渦結構。結果顯示負位渦在強渦旋中心上層產生之壓力擾動往周圍擴散，但在強渦旋中心則傾向垂直擴散。此外我們也利用 2020 年七月之月平均 ERA5 再分析資料對於：1) 落磯山脈 2) 青康藏高原做位渦反演；利用 2015 年 7 月 20 日 00UTC-24UTC 之每小時 ERA5 再分析資料對於 3) 鄰近台灣之鋒面個案做位渦反演。落磯山脈的三維位渦反演結果整體與觀測吻合，如反演場之低層噴流強度與延伸範圍皆與觀測十分吻合。青康藏高原的三維位渦反演結果則能部分捕捉如索馬利噴流和高原東側南風等特徵。此外，我們在落磯山脈的反演中分離上層與下層動力條件，其線性疊加後之結果與原反演場幾乎一致，這顯示了位渦反演可用於分離特定位渦在地形附近對整體反演平衡場之重要性。另一方面，台灣個案平衡模式中層大氣位渦反演的風速比起觀測的風速小約 16%，顯示在一天的時間尺度下平衡場在觀測場中的重要性。反演的低層西南風場展現空間均勻性，風速區並往西南方向延伸，這特性和觀測一致，也顯示位渦動力的重要性。

本研究包含：

1. 建構地形約束下之線性平衡與非線性平衡等熵座標平衡模式；模式可以在等熵座標下處理地形與地表斜壓性
2. 分析地表暖心結構以及地形冷卻作用，得出兩者對於低層噴流強度影響為線性關係
3. 分析低層逆溫層對低層噴流強度之影響；在地形之上的逆溫層會增強低層噴流強度
4. 非線性平衡下類颱風位渦反演，並探討高層與低層暖心結構下壓力擾動分布
5. 以 ERA5 再分析資料為基礎，反演落磯山脈，青康藏高原，及台灣附近西南氣流之平衡場；反演結果與觀測場部分相似。

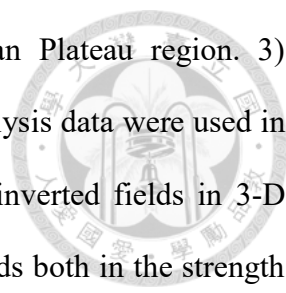
關鍵詞：位渦、反演原理、無質量層、非線性平衡反演、落磯山脈、青康藏高原、台灣附近西南氣流

Abstract



Potential vorticity (PV) contains information on the dynamical and thermal properties of the atmosphere. With hydrostatic balance approximation and horizontal wind balance relation, the balanced wind and the temperature information can be retrieved solely from PV field. This retrieval is often called the PV inversion or the invertibility principle of PV. The PV inversion often involved solving an elliptic partial differential equation with the nonlocal solution that is global in the domain. The PV inversion is a powerful method to recover balanced horizontal motions and vertical temperature structure. This thesis studies the topographically bound balanced motion with isentropic coordinate. Namely, we study the balanced motion in the presence of the topography with temperature intersection. We applied “massless layer approach” in our models, which can solve invertibility problems that isentropes intersect with ground or topography.

Our approach mainly followed the work from the two-dimensional linear balanced modeling of Silvers and Schubert (2012) and Fulton et al. (2017). We have built both linear and nonlinear balanced models in the three-dimensional geometry with the isentropic coordinate. With such balanced model and massless layer approach, we studied idealized numerical simulations in 2-D and 3-D geometries. The dynamics of LLJs in Silvers and Schubert (2012) are reproduced and further gave a quantitative analysis of the effect from both thermal and orographic forcing. Additionally, we found that the low-level inversion layer can enhance or weaken the strength of the LLJs depending on whether the inversion layer touches the topography. For a 3-D invertibility, we found that the flow strength of the LLJs would be weaker than a 2-D case. The nonlinear balanced model is for the typhoon-like vortex invertibility. The pressure perturbations in a strong and in a small vortex structure is studied. Stronger vortex allows a stronger pressure perturbation. Finally, we performed real case PV



inversions in: 1) The Rocky Mountains regions and 2) the Tibetan Plateau region. 3) southwesterly flow near Taiwan island. ERA5 Monthly averaged reanalysis data were used in 1) and 2) while ERA5 hourly reanalysis data were used in 3). The inverted fields in 3-D geometry near the Rocky Mountains highly resemble the observed fields both in the strength and the spatial distribution of the LLJs. Besides, the superposition of the upper-level and lower-level dynamics wind fields in the Rocky Mountains case implies that we can trace the influence of PV source near the topography, which manifest the importance of the PV invertibility principle. The inverted fields near Tibetan Plateau partially captured the features in observation like the occurrence of Somali jet and the southerly at the east of plateau. On the other hand, the balanced models underestimated the wind speed of southwesterly flow only about 16% near Taiwan, which reminds us that in daily time-scale balanced wind fields might be important. The low-level south-easterly near Taiwan is smooth and extend southwestwards, which is consistent with observations and reveals that PV dynamics is important.

Keywords: Potential vorticity, invertibility principle, massless layer, nonlinear balance invertibility, Rocky Mountains, Tibetan Plateau, Southwesterly near Taiwan

Contents



誌謝	I
摘要	II
Abstract.....	IV
Contents	VI
LIST OF FIGURES	VIII
LIST OF TABLES.....	XIII
Introduction.....	1
1.1. Potential Vorticity Dynamics.....	1
1.2. Invertibility Dynamics.....	2
Formulation	6
2.1. Hierarchy of Potential Vorticity.....	6
2.2. Invertibility Principle and Massless Layer.....	7
2.3. Balance Relation	9
2.4. Boundary conditions and reference state	10
Idealized Numerical Experiments	13
3.1. Two-dimensional idealized invertibility Problems	13
3.2. Three dimensional invertibility Problems	16
3.3. Nonlinear Balanced Invertibility Models	16
Real Case Numerical Experiments.....	19
4.1. The Rocky Mountains Observations and Diagnosis.....	19
4.2. The Taiwan and Tibetan Observations and Diagnosis	22
Conclusions.....	24
Bibliography	26
Appendix.....	28
A. Model Discretization.....	28
B. Model Convergence rate Experiments.....	31

C. Nonlinear Balance Model Solution.....35
Figure.....37



LIST OF FIGURES



Figure 1. The schematic diagram for how topography boundary conditions change isentropes in isobaric and isentropic coordinates. (a) Uniform grids on isentropic coordinate. The topography is invisible if we focus on the isentropes. (b) In pressure coordinate, isentropes bend upward due to topography (cooling effect).....37

Figure 2. The schematic diagram for how isentropes intersect with ground in isobaric and isentropic coordinates. (a) Uniform grids on isentropic coordinate. The grey shaded region is massless layer. (b) In pressure coordinate, isentropes bend downward due to surface temperature anomaly .38

Figure 3. The schematic diagram for the isentropic model. The governing equations and the boundary conditions are shown. The gray shaded region represents massless layer area which different governing equation is applied.39

Figure 4. The reference state of PV field as a function of θ , computed from (34). The Coriolis coefficient is set as $f = 7.3 \times 10^{-5} \cong 2\Omega \sin 30^\circ$40

Figure 5. Meridional wind field (shading) in (a) isobaric coordinate with θ (contour, in K) and (b) isentropic coordinate with pressure (contour, in hPa) under the effect of topography $\Phi_0 = 1200$ km. The LLJs are with anti-symmetric and anti-cyclonic patterns near the mountain, with maximum anticyclonic flow up to 11.3 m/s.41

Figure 6. As in Figure 5, but with surface temperature anomaly instead of topography. Near the thermal forcing region, the cyclonic flow is induced with wind speed up to 20.4 m/s.42

Figure 7. As in Figure 5, but with both surface heating $\theta_0 = 6.5$ K and topography $\Phi_0 = 1200$ km. There is nearly no wind in physical domain. The maximum value $v = 0.69$ m/s.43

Figure 8. As in Figure 5, but with both surface heating $\theta_0 = 11$ K and topography $\Phi_0 = 1200$ km. The low-level jets have anti-symmetric and cyclonic patterns near the heating mountain, with maximum value $v = 8.0$ m/s.44

Figure 9. The relation between Gaussian-Shaped topographic forcing and surface thermal forcing. (a) width = 1000 km, $v_{max} = 0.1 + 1.9\Delta T - 0.01\Delta H$, with $R^2 = 0.9984$ (b) width = 2000 km, $v_{max} = 0.1 + 1.8\Delta T - 0.01\Delta H$, with $R^2 = 0.9969$. The forcing effects are quite linear and nearly independent of the width of the mountain.45

Figure 10. PV anomaly as inversion layer (shading, in PVU) and isentropes

(contour, in K) in pressure coordinate. Inversion layers locate in (a) 297.5 K (b) 305 K (c) 340 K.....	46
Figure 11. Wind difference from Figure 8 (a) due to the existence of inversion layer (shading, in m/s) and isentropes (contour, in K) in pressure coordinate. Inversion layers locate in (a) 297.5 K (b) 305 K (c) 340 K.....	47
Figure 12. (a) Vertical profiles of PV for no inversion layer (solid line), low-level inversion (Dashed line), mid-level inversion (Dotted line), and high-level inversion (Dash-dot line). (b) the maximum wind speed change as a function of θ level where inversion layer located. Note that there is maximum wind speed when the inversion layer being at $\theta = 305$ K.....	48
Figure 13. (a) Wind speed (shading), wind vector (quiver), and θ (contour) at 900hPa. (b) As in Figure 8(a), but we solved a 3-D invertibility problem. Both with circular surface thermal forcing $\theta_0 = 11$ K and orographic forcing $\Phi_0 = 1200$ km but with the governing equation being (41). The maximum wind is 5.7 m/s. Note that the magnitude of the LLJs is smaller than a 2D source case.	49
Figure 14. As in Figure 13, but with meridionally symmetric conditions. The maximum wind is m/s. Note that the magnitude of the LLJs significantly decreases compared to a 2-D source case.	50
Figure 15. The maximum meridional wind for different aspect ratio. The dash line is a 2-D source case which the wind speed is maximized.	51
Figure 16. Numerical results for (a) linear balance (b) nonlinear balance relation in weak PV anomaly experiments, including induced cyclonic flow (shading, in m/s) and pressure (contour, in hPa). The maximum wind speeds are (a) 5.5 m/s (b) 5.1 m/s, respectively.	52
Figure 17. Numerical results for nonlinear balance relation invertibility. (a) A strong typhoon-like PV anomaly (shading, in PVU) (b) Induced cyclonic flow (Shading, in m/s) and pressure (contour, in hPa). The maximum wind speed is 32.1 m/s, which located in about 70 km in radius and rapidly decays as height and radius increase.....	53
Figure 18. Numerical results for (a) linear balance (b) nonlinear balance relation in strong typhoon-like PV anomaly experiments, including induced cyclonic flow (shading, in m/s) and pressure (contour, in hPa). The maximum wind speed and minimum pressure are (a) 49.0 m/s and 995 hPa (b) 32.1 m/s and 976 hPa, respectively. Both of their maximum wind speeds are located in about 70 km. Note that significant center warming and pressure fall occur only when gradient wind balance is applied.	54
Figure 19. The invertibility problem with extra upper negative PV anomaly. (a) PV	

anomaly (shading, in PVU) (b) Wind and pressure difference with Figure 18 are presented in shading and contour, respectively. Note that the maximum pressure difference appears right below negative PV anomaly and decays as the height decrease.	55
Figure 20. As in Figure 19, but with meridionally symmetric conditions. Note that the maximum pressure difference appears right above the positive PV anomaly and spreads more in vertical direction than in Figure 19.	56
Figure 21. (a) Mean wind (quiver, in m/s) averaged over July, 2020 from ERA5 reanalysis data at (a) 200hPa (b) 925hPa level. The shading is (a) PV field (in PVU) and (b) elevation (shading, in meter). The contour in (b) is potential temperature.	57
Figure 22. (a) Mean cross sections of meridional wind (shading, in m/s) averaged over the latitude sector 30-35° N from ERA5 reanalysis data and (b) interpolation to longitude-potential temperature cross sections from (a). Contour is (a) isentropes (in K) (b) isobars (in hPa). Black region is topography and gray shading is the domain out of the physical region. Here we choose $p = 1000, 150$ hPa. We can identify cyclonic LLJs patterns near The Rocky Mountains.	58
Figure 23. (a) Mean cross sections of PV (shading, in PVU) averaged over the latitude sector 30-35° N from ERA5 reanalysis data and (b) interpolation to longitude-potential temperature cross sections from (a). Contour is (a) isentropes (in K) (b) isobars (in hPa). Black region is topography.	59
Figure 24. Meridional wind field (shading) in (a) isobaric coordinate with θ (contour) and (b) isentropic coordinate with pressure (contour). Black region in (a) is topography and we choose the domain out of $p=(1000\sim 150)$ hPa). The patterns of wind field are similar with observations (Figure 22).	60
Figure 25. As in Figure 24, but with θS and the top pressure assigned by interpolation. The patterns of wind field are similar to observations (Figure 22), but too large southerly at the east of The Rocky Mountains.	61
Figure 26. As in Figure 25, but with smaller θS slope at the east of the mountain. The wind field is more like observations (Figure 22).	62
Figure 27. The cross section of meridional winds (shading, in m/s) and θ (contour, in K) at 35°N for the 3-D balanced model results. Lift massless layer temperature for (a) 0hPa (b) 25 hPa (c) 50 hPa. The black region is topography. Their northerly wind speed at the west of the mountain is up to (a) 18 m/s (b) 16 m/s (c) 12 m/s.	63
Figure 28. (a) The wind difference (shading, in m/s) between lifting massless layer for 50 hPa and 0 hPa and (b) the PV field (shading, in PVU). Thin contours	

are interpolated pressure. Depicting domains are between $\theta = 295$ K and $\theta = 325$ K. Solid, dotted, and dash lines are for no lifting, 25 hPa lifting, and 50 hPa lifting, respectively.....	64
Figure 29. The horizontal wind fields (quiver, in m/s) and θ fields (shading, in K) at 875 hPa for the 3-D balanced model results near the Rocky Mountains. Lifting massless layer temperature for (a) 0hPa (b) 25 hPa (c) 50 hPa. The black region is topography.	65
Figure 30. Meridional wind fields (shading, in m/s) in isobaric coordinate with θ (contour, in K). (a) Upper dynamics case. The PV field value below 330 K is zonally averaged and the topography and surface thermal forcing is set to be zero. (b) Lower dynamics case. The PV field value above 330 K is zonally averaged. (c) the summation of upper dynamics and lower dynamics wind field. Note that in convenience we directly applied the pressure contour of lower dynamics in (c).....	66
Figure 31. (a) Mean wind field (quiver, in m/s), potential temperature at 700 hPa, and elevation (shading, in meter). (b) Wind field (quiver, in m/s) and PV (shading, in PVU) at 200 hPa. All fields are averaged over July, 2020 from ERA5 reanalysis data.	67
Figure 32. Mean wind field (quiver, in m/s) and potential temperature (shading, in K) at 700 hPa. Lifting massless layer temperature for 50 hPa is used in this result.....	68
Figure 33. (a) Observation (b) numerical result for the cross section of u wind (shading, in m/s) and potential temperature (contour, in K) at 90°E.	69
Figure 34. (a) Observation (b) numerical result for the cross section of u wind (shading, in m/s^{-1}) and potential temperature (contour, in K) at 30°N.....	70
Figure 35. (a) Mean wind field (quiver, in m/s) and PV field (shading, in PVU) at 500 hPa. (b) Wind field (quiver, in m/s) and temperature (shading, in K) at 850 hPa near Taiwan. All fields are averaged from 0000 UTC to 2400 UTC on 20 July 2015 from ERA5 hourly reanalysis data.	71
Figure 36. Cross sections of PV (shading, in PVU) and potential temperature (contour, in K) at 23°N from ERA5 reanalysis data. This cross section contains the Taiwan island.	72
Figure 37. (a) Observed fields (b) numerical results for cross sections of v wind (shading, in $/s^{-1}$) and potential temperature (contour, in K) for 23°N near Taiwan. Note that massless layer temperature θ_s are lifting for 50 hPa. The maximum southerly is about (a) 19.2 m/s (b) 16.5 m/s	73
Figure 38. (a) Mean wind field (quiver, in m/s) and PV field (shading, in PVU) at 500 hPa. (b) Wind field (quiver, in m/s) and temperature (shading, in Kelvin)	

at 850 hPa near Taiwan. The position of the Taiwan island is at about $x, y = 100, 300$ km. Note that massless layer temperature θ_s are lifting for 50 hPa.

.....	74
Figure A.1. The wind difference for Fig 8 as residual decrease. (e.g. abscissa $RES = 10^{-2}$ means that the u_{max} which residual is equal to 10^{-2} minus the u_{max} which residual is equal to 10^{-1}).....	30
Figure B.1. The vorticity (shading, in 1/s) and the streamfunction (contour)	33
Figure B.2. Schematic diagram for error smoothing (relaxation) processes. It is shown that after several error smoothing procedures, the initial low wave number error (in green solid line) decrease slowly (in green dashed line). However, initial high wave number error (in blue solid line) dissipates quickly (in blue dashed line).....	33
Figure B.3. Residual versus model run time. Black, blue, and red line represent Jacobi iterative method, multigrid method (see Fulton et al. 1986), and interpolation method, respectively.....	34
Figure C.1. A snapshot for unstable relaxation case. In nonlinear Jacobian term dominating situations, the relaxation method may somehow result in the error smoothing process fails and the model diverge.....	36

LIST OF TABLES

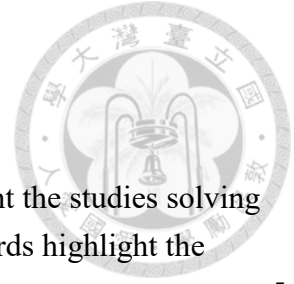


Table 1. Invertibility problem categories. Blue words highlight the studies solving invertibility with massless layer approach and stared words highlight the studies solving invertibility with topography.....	5
Table 2. The model resolutions and the residual as criteria for the convergence of models	30

CHAPTER 1

Introduction

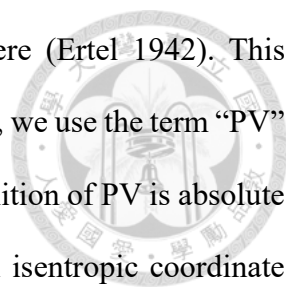


1.1. Potential Vorticity Dynamics

PV balanced dynamics are relatively slow-varying although the atmosphere on Earth essentially possesses dynamics with multiply time and space scale. Hence, PV is a useful tool to analyze the balanced dynamics of the atmosphere. There are two main principles of PV dynamics: 1) PV conservation and 2) PV invertibility principles (Hoskins et al. 1985). PV conservation principle predicts the evolution of PV fields under the Lagrangian perspective. However, if we wish to realize PV evolution with a given PV field under the Eulerian perspective, PV invertibility principle, or PV inversion must be included.

During the early stage of investigating vorticity, Rossby and Charney (Hoskins et al. 1985) proposed that we can treat large-scale atmosphere motions as the evolution of the vertical absolute vorticity ζ_a on 2-D planes. The benefits of this idea are obvious. Absolute vorticity, including both the rotational effect of Earth and fluid, is materially conserved in non-divergent conditions. The flows can be obtained easily by solving Poisson's equation. However, if we take the horizontal divergence into consideration, the material conservation of ζ_a would be spoiled. Therefore, the concept of potential vorticity (PV) was created for catching up the deficiency of merely discussing vorticity. Since PV contains information about the thickness of the fluid, the change of vorticity resulted from stretching can be captured. The widely use of PV implies that the creation of vorticity by stretching as well as the horizontal transport of vorticity mostly determine the vorticity budget (Hoskins et al. 1985).

The utilization of PV is an effective way to understand atmospheric dynamics in the quasi-geostrophic theory framework. Quasi-geostrophic PV (QGPV) dynamics can be applied to multiply layer models to study many features of large-scale meteorological phenomenon, for example, baroclinic instability. Nevertheless, in addition to QGPV, fully 3-D version of PV is



proposed to better exploit the continuous properties of the atmosphere (Ertel 1942). This category of PV is referred to as “Ertel potential vorticity”. For simplicity, we use the term “PV” to refer to Ertel potential vorticity in the following discussion. The definition of PV is absolute vorticity per mass in two potential temperature layers. PV along with isentropic coordinate (take potential temperature as vertical coordinate) have many merits. For example, potential temperature is a conserved quantity under adiabatic processes. Even in the presence of diabatic heating, Lagrangian view of general circulation can be achieved. In such perspective, Hadley cells, Ferrel cells, and polar cells can be regarded as one single cell, which is driven by thermal forcing in tropical regions (Gallimore and Johnson 1981). As a temperature coordinate, isentropic coordinate is suitable for solving frontogenesis problems (Fulton and Schubert 1991). PV can be conserved (Guinn and Schubert 1994) under dry adiabatic processes. Furthermore, if we apply isentropic coordinate, due to the conservation of potential temperature, PV would be conserved in 2-D motions (Hoskins 2015).

1.2. Invertibility Dynamics

We can appreciate the most essence of PV dynamics as written down in Hoskins et al. (1985):

“the significance of potential vorticity does not end with its importance as an air-mass tracer. It is also the key to a very powerful and succinct view of the dynamics. IPV maps, in particular, are a natural diagnostic tool well suited to making dynamical processes directly visible to the human eye and to making meaningful comparisons between atmospheric models and reality.”

Although Kleinschmidt’s work as “an extremely important piece of pioneering”, in Hoskins et al. (1985), the concept of invertibility principle was generalized and regarded as one of important parts of balanced dynamics.

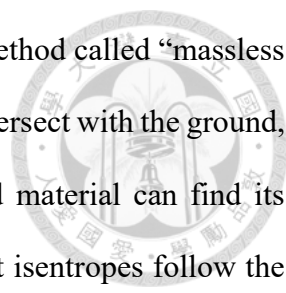
Eliassen (1980) investigated the invertibility problem for topographically bounded, balanced, and stratified fluid. They calculated “the critical height” in 2-D orography and

qualitatively discussed the 3-D invertibility problem. When the ridge of topography exceeds this height, the linear theory (constant density) would break down. Although the restriction of isopycnic bottom conditions, this study is a milestone that they made use of the exact potential vorticity theorem instead of quasi-geostrophic vorticity.

Schubert and Alworth (1987) explored the evolution of PV in tropical cyclones. As previously mentioned, the evolution of PV contains conservation and invertibility principles. In order to make the time evolution of PV be obtained directly, they derived the flux form of the potential density equation (the reciprocal of PV), which bears the advantage that if the source of angular momentum and diabatic heating is given. Then, by assuming particular heating profiles, analytical solutions can be obtained. However, to retrieve wind fields, numerical solutions of the nonlinear invertibility problem should be solved. The results were similar to observations.

The combination of isentropic and potential latitude coordinates makes PV local conserved (Schubert et al. 1995). In such a scenario, with initial mass distribution (PV perturbations) given by mixed layer model theory, invertibility principle problems are solved and the meridional slope of trade wind inversion layer is predicted. The slope given by the balanced model is much smaller than the slope of the initial mass distribution. Such a result can be dynamically explained as PV invertibility principle tends to smooth the gradient of mass and wind response.

Yet, although the application of isentropic coordinate along with other conserved horizontal coordinate make prognostic equation free from dealing with advection, some limitation still exists. If the lower boundary is not an isentropic surface, in physical space some of the isentropes would intersect with ground. In this case, below a specific vertical height (cooler than the surface potential temperature) exists regions where do not correspond to any real fluid material. In other words, the invertibility would be ill-defined if the lower boundary is not an isentropic surface.



To handle this situation, Fulton and Schubert (1991) proposed a method called “massless layer approach”. In this method, they imagined that when isentropes intersect with the ground, it follows the surface instead of disappearing. Therefore, every fluid material can find its correspondence in isentropic coordinates. However, in the regions that isentropes follow the physical surface, a different governing equation should be applied. The detail of the massless layer approach would be discussed in CHAPTER 2. With the massless layer approach, they gave solutions to surface frontogenesis processes based on IPV modeling, which is comparable to the results of Hoskins (1982).

The massless layer approach is also used in Silvers and Schubert (2012) and Fulton et al. (2017). Silvers and Schubert (2012) attributed the western and eastern parts of the LLJs to the isentropic surfaces intersecting with the topography. They solved the invertibility principle and demonstrated that if the surface thermal forcing overcomes orographic forcing, cyclonic flow centered on the topography would be induced. These flow patterns match well with the basic features of observed LLJs like the maximum speed and rapidly decaying in the vertical and horizontal direction. Fulton et al. (2017) studied the strong easterly near Antarctica, indicated that the strong easterly is induced by the combined effect of high PV anomaly and orographic cooling effect. Besides, they added another PV source, including low latitude surface temperature gradient in mid-latitude, upper-level pressure gradient in upper-level, and stratosphere PV source in upper-level. The inverted wind and mass fields are quite similar to observations. Both studies successfully explained the observed field by balanced dynamics, which provides us a precious experience to diagnose topographic-related balanced dynamics.

In this study, we mainly follow the concept of model construction from Silvers and Schubert (2012) and Fulton et al. (2017). **In Chapter 2**, we focused on the PV inversion problems, especially in the framework of PV fields in isentropic coordinate. The governing equation, the boundary conditions, and the realization of the massless layer in the invertibility model would be introduced. **In Chapter 3**, idealized numerical simulations in 2-D and 3-D

geometries were performed and analyzed. Especially, in the 3-D invertibility problem, nonlinear balance relation was applied and a typhoon-like case was studied. In **CHAPTER 4**, we solved 2-D and 3-D invertibility problems with PV fields and boundary conditions from ERA5 reanalysis data. In **CHAPTER 5**, we concluded our work.

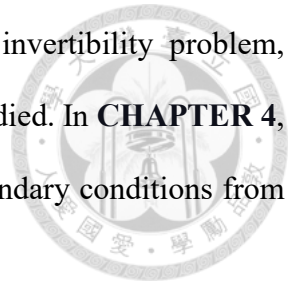


Table 1. Invertibility problem categories. Blue words highlight the studies solving invertibility with massless layer approach and starred words highlight the studies solving invertibility with topography.

	Linear balance	Nonlinear balance
Cartesian geometry	Eliassen 1980 Silvers and Schubert 2012* Fulton and Schubert 1991	
Cylindrical geometry		Schubert and Alworth 1987 Fulton et al. 1995
Spherical geometry (full Coriolis force)	Fulton et al. 2017*	Schubert et al. 1995

CHAPTER 2

Formulation



2.1. Hierarchy of Potential Vorticity

Start from 2-D nondivergent vorticity equation:

$$\frac{d\zeta_a}{dt} = 0, \quad (1)$$

where the simplest conserved quantity

$$\zeta_a = f + \zeta. \quad (2)$$

We can always express vorticity in terms of ψ by the following definition

$$\begin{cases} u = -\frac{\partial\psi}{\partial y} \\ v = +\frac{\partial\psi}{\partial x} \end{cases} \quad (3)$$

and obtain a poisson's equation

$$\zeta_a = f + \nabla^2\psi, \quad (4)$$

which is an elliptic partial differential equation with uniform coefficients. Fourier transform would be an efficient way to solve equation (4). In higher hierarchy, divergent barotropic fluids can be described by

$$\frac{d\zeta_a}{dt} + \zeta_a \left(\frac{\partial u}{\partial x} + \frac{\partial v}{\partial y} \right) = 0 \quad (5)$$

and for incompressible fluids the continuity equation is

$$\frac{\partial h}{\partial t} + \frac{\partial hu}{\partial x} + \frac{\partial hv}{\partial y} = 0. \quad (6)$$

Combining the vorticity equation with the continuity equation, the conservation of PV appears

$$\frac{dP}{dt} = 0, \quad (7)$$

where P is PV. PV in QG system can be written as

$$P = \frac{f + \nabla^2 \psi}{h}. \quad (8)$$

When the depth of the fluid column h increases, according to the continuity equation, the fluids must be stretched due to the horizontal flows converge, and hence, the absolute vorticity increases as well.

The discussion above regards the atmosphere as vertically homogeneous fluids. However, Hoskins et al. (1985) pointed out that in isentropic coordinate the depth can even represent the mass per two isentropes. This idea was described by

$$P = \frac{\vec{\zeta}_a \cdot \nabla \theta}{\rho}, \quad (9)$$

which is just Ertel potential vorticity (PV) as mentioned in CHAPTER 1. Furthermore, in large-scale dynamics, the vertical component of vorticity is first important, and the PV equation can be described by

$$P = \frac{f + \zeta_\theta}{-\frac{1}{g} \frac{\partial p}{\partial \theta}}. \quad (10)$$

2.2. Invertibility Principle and Massless Layer

To solve PV invertibility problems, we need to derive an equation which contains the balanced wind and the temperature information. Start from the definition of Ertel potential vorticity (10) and Exner function:

$$\Pi = c_p \left(\frac{p}{p_0} \right)^\kappa, \quad (11)$$

where f is Coriolis force, $\zeta_\theta = (\partial v / \partial x)_\theta - (\partial u / \partial y)_\theta$ is vorticity on isentropes, $\kappa = R_d / c_p$, and $-1/g (\partial p / \partial \theta)$ is static stability parameter. We aim to transform it into the equation which is a function of (x, y, θ) instead of (x, y, p) . Π serves as the state of the atmosphere ($\partial M / \partial \theta = \Pi$ corresponding to $\partial \Phi / \partial p = -R_d T / p$). Our goal is to eliminate p in (10). By the relation $\Pi \theta = c_p T$, we can eliminate T as well. To accomplish this, we apply the chain rule:

$$\frac{\partial p}{\partial \theta} = \frac{\partial \Pi}{\partial \theta} / \frac{d\Pi}{dp}. \quad (12)$$

Note that Exner function is a function of pressure only: $\Pi = \Pi(p)$.

Then differentiating $\Pi(p)$ with p , we obtain:

$$\frac{\partial p}{\partial \theta} = \frac{p}{\kappa \Pi} \frac{\partial \Pi}{\partial \theta}. \quad (13)$$

With the relation:

$$\Pi \theta = c_p T = \frac{p}{\kappa \rho} \quad (14)$$

or:

$$p = \kappa \Pi \theta \rho, \quad (15)$$

we can replace p in equation (13) and finally write pressure as a function of θ :

$$\frac{\partial p}{\partial \theta} = \rho \theta \frac{\partial \Pi}{\partial \theta}. \quad (16)$$

Now we can rewrite (11), and obtain invertibility principle:

$$\frac{g}{\theta \rho P} (f + \zeta_\theta) + \frac{\partial \Pi}{\partial \theta} = 0. \quad (17)$$

Furthermore, according to (3), we can express ζ_θ in terms of ψ and obtain

$$\frac{g}{\theta \rho P} (f + \nabla^2 \psi) + \frac{\partial \Pi}{\partial \theta} = 0. \quad (18)$$

Given that an extra equation describes the relation between Π and ψ and proper boundary conditions are applied, the solution can be uniquely determined. The discussion above is enough to determine solutions if we only wish to solve invertibility problems that topographic surface follows an isentropic surface (like Figure 1).

However, if we want to solve invertibility problems in the real world, we probably need to treat the tricky mathematical issue: the isentropes intersect with ground, as shown in Figure 2(a). The massless layer approach was proposed as a method to solve the invertibility principle in isentropic coordinates without complex a lower boundary condition (Fulton and Schubert 1991). This method physically images that when the isentropic surfaces touch the ground, they



follow the topography. Hence, in such a picture, every point in (x, y, θ) coordinate space is defined (Figure 2a). However, as Figure 2 (b) shown, several isentropes in massless layer overlap in physical space. There is no mass between such two isentropes, which indicates that the first term in (17) should vanish like

$$\frac{(f + \zeta_\theta)}{P} = -\frac{1}{g} \frac{\partial p}{\partial \theta} = 0. \quad (19)$$

As a result, equation (18) becomes

$$\frac{\partial \Pi}{\partial \theta} = 0. \quad (20)$$

To separate the massless layer region from atmosphere region, we need to specify surface potential temperature $\theta_S(x, y)$, as shown in Figure 3. The regions below $\theta = \theta_S(x, y)$ are massless layer and should apply (20) as one of the governing equations.

2.3. Balance Relation

To solve the invertibility principle, we need to make connection between vertical structure (Π) and horizontal flow (ψ). We assume that balance motions follow hydrostatic equilibrium, which in θ -coordinate can be written as:

$$\Pi = \frac{\partial M}{\partial \theta}, \quad (21)$$

where M is Montgomery stream function:

$$M = c_P T + \Phi. \quad (22)$$

Substitute (21) into (18) and (20), we obtain governing equations

$$\begin{cases} \frac{g}{\theta \rho P} (f + \nabla^2 \psi) + \frac{\partial^2 M}{\partial \theta^2} = 0 & \text{in atmosphere} \quad - \\ \frac{\partial^2 M}{\partial \theta^2} = 0 & \text{in massless layer.} \quad - \end{cases} \quad (23)$$

To introduce the different hierarchy of balance relations, we start from horizontal momentum equation in isentropic coordinate

$$\frac{\partial \vec{V}}{\partial t} + \vec{V} \cdot \nabla \vec{V} + f(\hat{k} \times \vec{V}) = -\nabla M. \quad (24)$$

Take the divergent of (24), we obtain

$$\begin{aligned} \frac{\partial \nabla \cdot \vec{V}}{\partial t} + \vec{V} \cdot \nabla (\nabla \cdot \vec{V}) + \left(\frac{\partial^2 u}{\partial x^2} + \frac{\partial^2 v}{\partial y^2} + \frac{\partial u}{\partial x} \frac{\partial v}{\partial y} + \frac{\partial v}{\partial x} \frac{\partial u}{\partial y} \right) \\ + \nabla \cdot (f \nabla \psi) = -\nabla^2 M. \end{aligned} \quad (25)$$

This complex equation (25) can be simplified if we make non-divergent assumption [like (3)]

$$2 \left[\frac{\partial^2 \psi}{\partial x^2} \frac{\partial^2 \psi}{\partial y^2} - \left(\frac{\partial^2 \psi}{\partial x \partial y} \right)^2 \right] + \nabla \cdot (f \nabla \psi) = \nabla^2 M, \quad (26)$$

which is called Bolin-Charney balance relation (or nonlinear balance relation for the following discussion). If we neglect nonlinear term on f -plane, we can obtain linear balance relation

$$f \nabla^2 \psi = \nabla^2 M. \quad (27)$$

With linear balance relation, we can substitute $\nabla^2 \psi$ in (27) into (28) and obtain the governing equations

$$\begin{cases} \frac{g}{\theta \rho P} \left(f + \frac{1}{f} \nabla^2 M \right) + \frac{\partial^2 M}{\partial \theta^2} = 0 & , \text{when } \theta \geq \theta_s \quad - \\ \frac{\partial^2 M}{\partial \theta^2} = 0 & , \text{when } \theta < \theta_s. \quad - \end{cases} \quad (28)$$

There is only one unknown variable and therefore we can solve for it theoretically.

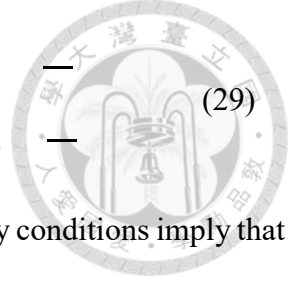
2.4. Boundary conditions and reference state

Equation (28) is solvable. However, to make the solution uniquely determined, we need to apply boundary conditions. Here we follow the setup of upper and lower boundary conditions in Silvers and Schubert (2012).

Although different governing equations are applied in different regions, (28) are essentially elliptic partial differential equations boundary conditions applied. For lateral boundary conditions (29), simple Neumann boundary conditions are applied

$$\begin{cases} \frac{\partial M}{\partial x} = 0 \\ \frac{\partial M}{\partial y} = 0 \end{cases}, \text{ at } x = \pm L_x \quad \text{---} \quad (29)$$

$$\begin{cases} \frac{\partial M}{\partial x} = 0 \\ \frac{\partial M}{\partial y} = 0 \end{cases}, \text{ at } y = \pm L_y. \quad \text{---}$$



where L_x and L_y are the horizontal range of the domain. Such boundary conditions imply that the flow at the boundaries is parallel to the direction of the boundary. In a 2-D geometry, it becomes zero wind at the boundaries. For upper boundary condition (30), we specify upper pressure and therefore obtain

$$\frac{\partial M}{\partial \theta} = \Pi(p_T) \quad , \text{ at } \theta = \theta_T, \quad \text{---} \quad (30)$$

where $\Pi(p_T)$ is defined in (11). Since we wish to investigate the orographic forcing, surface thermal forcing, and massless layer dynamics, the choice of lower boundary condition is crucial.

To satisfy the surface geopotential, we make subtraction between M and $\frac{\partial M}{\partial \theta}$ at $\theta = \theta_B$, and we have (31)

$$M - \theta \frac{\partial M}{\partial \theta} = \Phi_S \quad , \text{ at } \theta = \theta_B, \quad \text{---} \quad (31)$$

where Φ_S is the geopotential height and should be specified. In summary, the invertibility problem contains (28)-(31). To solve for M , we should specify $L_x, L_y, \theta_T, \theta_B, \theta_S, \Phi_S$, and P .

Since in balanced flow M monotonically increases with θ , to further make the solution easy to understand, we assume a reference state. This reference state decomposes Montgomery streamfunction into the background part and deviation from background part

$$M = \tilde{M}(\theta) + M'(x, y, \theta), \quad (32)$$

where the background part is a function of θ only. Furthermore, we specify

$$\tilde{M}(\theta) = \Pi(p_B) \theta - [\Pi(p_T) - \Pi(p_B)] \frac{(\theta - \theta_B)^2}{(\theta_T - \theta_B)^2}. \quad (33)$$

This reference state promises that $\tilde{\Pi}(\theta_B) = \Pi(p_B)$ and $\tilde{\Pi}(\theta_T) = \Pi(p_T)$, where $p_T = 150$ hPa and $p_B = 1000$ hPa in the following experiments unless otherwise noted. With (33), the reference state of Exner function is linearly increases along θ -coordinates. With such a

reference state assumption, we can construct a reference state of PV, which can be the PV field in a stationary atmosphere

$$\tilde{P}(\theta) = \frac{f}{-\frac{1}{g} \frac{d\tilde{p}}{d\theta}}. \quad (34)$$

The PV fields in CHAPTER3 are specified as (34) unless otherwise noted.

The reference state implies that the local relation between pressure and potential temperature. However, it can be proved that the reference state cannot affect the results of model. Once PV field and boundary conditions given, the reference state can make solutions converge faster.

CHAPTER 3

Idealized Numerical Experiments



To understand the basic PV invertibility dynamics, we simulated several idealized invertibility problems: 1) the formation and the strength of LLJs by the combination of topography effect and massless layer, 2) PV disturbance test, and 3) the effect of inversion layer coupled with topography. Moreover, we aimed to make dynamical explanations of the LLJs near The Rocky Mountains as discussion for real case. In this chapter, we set the domain parameters as $L_x = 7000$ km, $L_y = 7000$ km, $\theta_T = 360$ K, and $\theta_B = 290$ K.

3.1. Two-dimensional idealized invertibility Problems

For simplicity we first consider meridionally symmetric invertibility problem. To solve this problem in two-dimensional space (x, θ) , the invertibility principle becomes

$$\begin{cases} \frac{g}{\theta \rho P} \left(f + \frac{1}{f} \frac{\partial^2 M}{\partial x^2} \right) + \frac{\partial^2 M}{\partial \theta^2} = 0 & , \text{when } \theta \geq \theta_S \quad - \\ \frac{\partial^2 M}{\partial \theta^2} = 0 & , \text{when } \theta < \theta_S \quad - \end{cases} \quad (35)$$

and

$$\frac{\partial M}{\partial x} = 0 \quad , \text{at } L = \pm L_x \quad - \quad (36)$$

and

$$\frac{\partial M}{\partial \theta} = \Pi(p_T) \quad , \text{at } \theta = \theta_T \quad - \quad (37)$$

and

$$M - \theta \frac{\partial M}{\partial \theta} = \Phi_S \quad , \text{at } \theta = \theta_B. \quad - \quad (38)$$

We first demonstrated pure orographic forcing case (like Eliassen 1980 and Silvers and Schubert 2012). There are no surface thermal forcing and no massless layer. The geopotential

on the lower boundary is specified as a Gaussian mountain

$$\Phi_S(x) = gHe^{-(x/x_0)^2}, \quad (39)$$

where the maximum height is $H = 1200$ m and the width is $x_0 = 1000$ km. The surface thermal forcing $\theta_S = 0$ K. The result is shown in Figure 5. In this case, the topographic surface is just an isentropic surface. From Figure 5 we can realize the presence of the mountain is equivalent to specifying bottom pressure as the surface of mountain. The nonlocal effect of PV invertibility extend the pressure anomaly to the ambient regions. Therefore, in isobaric coordinate, the isentropic surface is bend upward to match the shape of mountain, which is equivalent to a cold region. Besides, according to thermal wind, we can expect anticyclonic flows near the topography.

In the pure isentropes intersect with ground case, we used a Gaussian forcing as well:

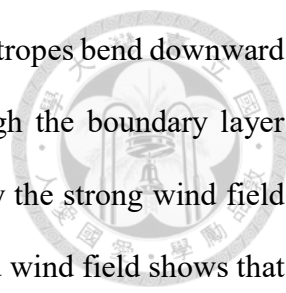
$$\theta_S = \theta_0 e^{-(x/x_0)^2}, \quad (40)$$

where the surface thermal forcing $\theta_S = 11$ K. and width $x_0 = 1000$ km. The numerical result is shown in Figure 6, which shows that the presence of surface thermal forcing makes the vertical pressure gradient vanish in massless layer and is equivalent to specifying the surface pressure just on the massless layer surface θ_S . The nonlocal effects of PV invertibility extend the pressure anomaly to the ambient regions. Therefore, in isobaric coordinate, the isentropic surface is bend downward and intersect with ground. That is equivalent to a warm region. According to thermal wind theory, we can expect cyclonic flows near the heating.

Although we can theoretically predict the flow direction, the real conditions on Earth are with the combination of orographic forcing (cooling) and surface thermal forcing (heating). To answer how the two forcings interact and what the net effect of them would be, the following paragraphs discuss another two idealized cases, in which we found thermal effect can cancel or even overcome orographic effect, as shown in Figure 7.

The induced LLJs are anti-symmetric and cyclonic with isentropes bend down, intersecting to the ground. The patterns are similar to observed heated mountain cyclonic flow like The





Rocky Mountains, as shown in section 4.1 (Figure 22), in which the isentropes bend downward and the strength of jets near the mountain are about 10 m/s. Although the boundary layer dynamics are not included in our invertibility problem, we can identify the strong wind field below and near 900 hPa. The resemblance between model and observed wind field shows that LLJs can be induced with a heated topography. The complete invertibility problem would be solved in CHAPTER4. The massless layer could be treated as a PV source in the domain. This idea may stem from Electromagnetism. As we known, charge generates electric fields. Such field act at a distance. With a given distribution of charge, we can solve for electric potential, which is one of the most classical invertibility problem. In finite domain invertibility problem, the charges outside the domain affect the electric field in the domain as well. Similarly, the massless layer and boundary conditions should be regarded as PV source and determine the mass and wind response in domain as well.

We also investigated the maximum cyclonic wind strength as a function of topographic forcing and surface thermal forcing, as shown in Figure 9. The results reveal that the PV invertibility principle we solved are quite linear. Besides, the strength of the LLJs is independent of the width of the mountain. We can explain this result physically by the argument that as the width of Gaussian mountain increases, the slope of the mountain decreases accordingly.

Additionally, to manifest how the change of PV influences inverted wind and mass fields, we gave idealized inversion layers as the form of PV anomalies based on the case that resembles the LLJs near the Rocky Mountains ($\theta_0 = 11$ K and $\Phi_S = 1200$ m) to examine how the different isentropic height of inversion layer affects the strength of cyclonic flow. The PV fields are shown in Figure 10 and the wind differences are shown in Figure 11. When the inversion layer penetrates the topography, the structure of the cyclonic flow is weakened, as shown in Figure 10 (a) and Figure 11 (a). The weakening of cyclonic flow could be explained by the PV anomaly being lacked in massless layer. This deficiency of positive PV is equivalent

to an anticyclonic flow and therefore cancel out the LLJs induced by bottom forcing. On the other hand, the inversion layer would interact with forcing and enhance cyclonic flow if it just touches with the topography. As the inversion layer lifting away from the topography gradually, the enhancement effect would decay. These processes are quantified, as shown in Figure 12. Note that 305 K is the maximum enhancement inversion layer height, which is slightly higher than $\theta_0 = 12$ K in (40).

3.2. Three dimensional invertibility Problems

The invertibility equation could be extended in a three-dimensional form as well

$$\frac{g}{\theta\rho P} \left(f + \frac{\partial^2\psi}{\partial x^2} + \frac{\partial^2\psi}{\partial y^2} \right) + f \frac{\partial^2\psi}{\partial \theta^2} = \frac{\overline{\sigma}}{\theta\overline{\rho}}. \quad (41)$$

We apply azimuthal symmetric orographic and surface thermal forcings, and the result is shown in Figure 13. The pattern of wind and thermal fields are similar to the results from a two-dimensional model, while the magnitude is smaller than the 2-D one. We can make an analogy of meridional symmetric PV source (2D) and azimuthal symmetric source (3D) as linear and point charge, which indicates that the streamfunction and corresponding gradient are smaller. This can be explained by equal partition principle. With extra dimension and corresponding term, the gradient in (41) would be smaller than the gradient in a 2-D case.

If the aspect ratio is increased from one (Figure 13) to infinite (Figure 14), the cyclonic LLJs would approach the 2-D limit (Figure 8). It is reasonable that (41) would resemble 2-D equation given that the variation of forcings along y-direction vanishes.

3.3. Nonlinear Balanced Invertibility Models

According to (26) and (23), we can solve the invertibility problem with a nonlinear balance model. Equation (37) and (38) are applied for the upper and lower boundary conditions. The reference state value assumptions are used for lateral boundary for nonlinearity-dominated case

$$M = \tilde{M}, \quad \text{at } L = \pm L_0. \quad (42)$$

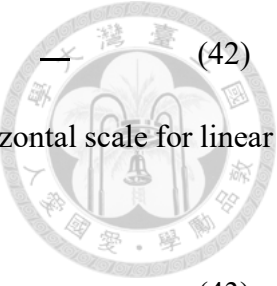
We first performed PV inversion that weak PV anomaly in high horizontal scale for linear and nonlinear cases. The PV anomaly is set as

$$P = P_0 e^{-\left[\left(\frac{r}{R}\right)^2 + \left(\frac{\theta}{\theta_0}\right)^2\right]}, \quad (43)$$

where $P_0 = 2$ PVU, $R = 400$ km, and $\theta_0 = 330$ K. The numerical result is shown in Figure 16. Simple scale analysis result shows that non-geostrophic component is one order less than geostrophic component. Therefore, the strength of vortex in nonlinear balance is slightly smaller in linear balance relation.

A typhoon-like case is simulated, whose $P_0 = 20$ PVU, $R = 50$ km, $\theta_0 = 290$ K. In this case, strong PV anomaly appears near surface in hurricane eye size. The results for linear and nonlinear invertibility are shown in Figure 17. The maximum wind speed appears at the radius about 70 km with a magnitude up to 32.1 m/s. We compared the difference between linear and nonlinear balance in this case, as shown in Figure 18. It is reasonable that the mass response in nonlinear balance relation is significantly larger than in linear balance since that in nonlinear balanced models the Rossby radius of deformation (c/ζ) can be quite small in high vorticity region according to the geostrophic adjustment theory. Similarly, the relatively small wind speed can be explained by that the pressure gradient force would be shared by both Coriolis force and centrifugal force in nonlinear balance relation. In summary, considering nonlinear balance instead of linear balance in an identical typhoon-like PV structure cases, the maximum wind speed decreases yet the warm core structure is prominent.

We added an upper-level negative PV anomaly with $P_0 = 1$ PVU, $R = 100$ km, and $\theta_0 = 360$ K, as an effectively upper troposphere warming. Such a PV profile is shown in Figure 19 (a). The difference between typhoon-like case and this case is shown in Figure 19 (b). Consequently, an upper-level anti-cyclonic flow is induced. The wind speed of such flow is up to 2 m/s and at the radius about 100 km. The pressure difference is positive since the air



with higher potential temperature extends to high pressure region. Note that the pressure difference spreads horizontally and vertically, while in high inertia stability region (about 340 K) the pressure difference spreads mainly vertically. Similarly, this is result from the small Rossby radius of deformation in the strong vorticity region.

To further demonstrate the influence of high inertia stability, we added a lower-level positive PV anomaly with $P_0 = 1$ PVU, $R = 100$ km, and $\theta_0 = 290$ K, as an effectively lower troposphere warming. Such a PV profile is shown in Figure 20 (a). The difference between typhoon-like case and this case is shown in Figure 20 (b). Consequently, a lower-level cyclonic flow is induced. The wind speed of such flow is up to 3 m/s and at the radius about 150 km. The pressure difference is positive since the air with higher potential temperature extends to high pressure region. Note that the pressure difference spreads more vertically than the case in Figure 19.

CHAPTER 4

Real Case Numerical Experiments



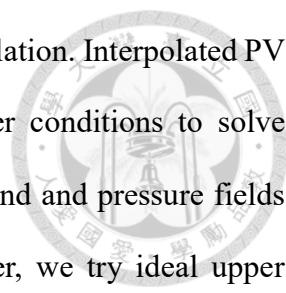
4.1. The Rocky Mountains Observations and Diagnosis

After understanding the invertibility and PV relations with several idealized cases discussed in CHAPTER 3, we demonstrate real cases invertibility in The Rocky Mountains with reanalysis data.

There are many observations about the warm seasons LLJs near the Rocky Mountains (Vera et al. 2006). One example of such feature is shown in Figure 21, where the lower-level cyclonic wind near The Rocky Mountains could be seen clearly. As shown in CHAPTER 3, the occurrence of the LLJs as well as the combination effect of topography and surface thermal forcing can be simulated by our balanced model. Figure 21 (b) also show that along the ridge the low-level wind and thermal fields are roughly meridionally symmetry, which may be a good example to demonstrate that invertibility principle with massless layer approach is suitable for the diagnosis of balanced dynamics both in ideal case and in real world environment.

To simplify our problem, we chose the area from 180°W to 40°W with the meridional mean from 30°N to 35°N in latitude. The obtained cross-section of wind and PV fields in pressure coordinate are shown in Figure 22 (a) and Figure 23 (a). The northerly (at east of the mountain, 6 m/s in maximum wind) is smaller in range and magnitude than southerly (at the west of the mountain, 10 m/s in maximum wind). Due to cool SST, there is local temperature minima at the east of mountain. Besides, the potential temperature is higher near the mountain, which is dynamically consistent with previous numerical results in CHAPTER3 (Figure 8). From the observed PV field, we notice that there is high PV region below 900hPa at the west of the mountain, which might intuitively explain the stronger wind speed there.

With topographical elevation data and surface temperature profile, the position of



isentropes intersected with ground [$\theta_s(x)$] can be determined by interpolation. Interpolated PV field, boundary conditions, and massless layer profile provide proper conditions to solve invertibility problem. We employed 2-D balanced model to retrieve wind and pressure fields and wished to obtain numerical results like observed fields. However, we try ideal upper boundary condition and massless layer profile to see if simple conditions can give similar patterns. The applied ideal massless layer profile as well as the numerical results are all shown in Figure 24. This profile is given by some simple combination of Gaussian function and linear function and PV field for invertibility is shown in Figure 23 (b). and the lower boundary conditions apply real topography the same as the black shading in Figure 22 (a). The lateral boundary conditions are set as (36).

There are several similarities between observations and numerical results. Near the center of topography, the cyclonic flow is captured although the extension of upper southerly. The upper-level patterns are also bear resemblance to the wind fields observed despite that the magnitude are significantly larger. Such result may due to the assumption of meridionally symmetry (Figure 21). The upper-level PV fields which originally tend to induce 3-D flow are employed to solve for 2-D invertibility problem. According to the previous 3-D idealized results (Figure 15), the strength of flow would be stronger

Next, we come back to more realistic case. We drew the massless layer profile through interpolated pressure profile, and used 300K as standard height to compute the surface pressure and then found out the corresponding massless layer temperature θ_s . The numerical results are shown in Figure 25, and the θ_s profile is also shown in the thick black line in Figure 25 (b). Although the lower-level features still exist, the southerly is too strong both in upper and lower atmosphere, especially in the east of the mountain.

Now we wish to match model results to observed fields better. we decrease the θ_s slope at the east of the mountain by giving a linear temperature gradient. The numerical results are shown in Figure 26, and the θ_s profile is also shown in the thick black line in Figure 26 (b).

The lower-level wind speed is reasonable than that in Figure 25. Although there is no simple and intuitive explanation for this adjustment, this result reminds us the importance of the lower boundary condition in determining inverted fields in whole domain. And for simplicity, we would demonstrate the influence of upper and lower dynamics based on these results.

To make inverted balanced fields match better with observed fields, we turned to 3-D invertibility (41) to include non-symmetric balanced dynamics near The Rocky Mountains. The horizontal domain is chosen as Figure 21. We apply the same method to obtain top and bottom boundary conditions but in two-dimensional form. The result is shown in Figure 27 (a). We notice that the magnitude of upper-level jets stream is weaker than those in two-dimensional model, which is close to observed value. However, the northerly at the west of the Rocky Mountains are still overwhelmed and extend to upper-level. This inconsistency may due to bottom boundary layer. In well mixed layer, stratification is small compared to free atmosphere. Therefore, PV field is small near ground.

We extra increase the height of massless layer for Figure 27 (b) 25hPa (c) 50 hPa. The lifted massless layer is shown in Figure 28. Obviously, the results of lifting massless layer for 50 hPa matches observations fields very well. The strength and spatial distribution of upper-level jets is well inverted. The overall low-level horizontal flow (Figure 29) is quite similar to observations (Figure 21 (b)). Despite that our model neglect the effect of boundary layer dynamics, the features of the LLJs near topography are well captured both in magnitude and thickness of jets. It is clear in Figure 28 (a) that lifting massless layer mainly affects the west of the mountain, where possesses high PV fluctuations as well as the lowest surface temperature. Both characteristics make interpolation less accurate. Similarly, in near ground area the reanalysis data are less convincing. Therefore, we can realize why lifting massless layer can produce patterns like observed fields.

Turn back to 2-D invertibility problem. To demonstrate the nonlocal effect of PV invertibility, we separated any PV source into upper and lower dynamics by 330 K height. The

result is shown in Figure 30. The upper dynamics case (Figure 30 (a)) mainly result from upper PV disturbance, while the lower dynamics (Figure 30 (b)) can mainly be attributed to orographic forcing and surface thermal forcing. Their wind fields summation is shown in Figure 30 (c). The prevalence of southerly in upper PV dynamics is canceled out by the strong northerly in lower dynamics case. The summation wind field is very closed to whole domain inversion in Figure 26. This result reveals that our invertibility equations are basically linear. This characteristic is an advantage when we wish to analyze the effect of local PV contribution.

4.2. The Taiwan and Tibetan Observations and Diagnosis

Previous research on balanced flow with topography about the strong easterly near the edge of Antarctica (Fulton et al. 2017), the cyclonic flow near Andes Mountains. In CHAPTER 4.1, we fully explore the real case 2-D and 3-D invertibility problem near The Rocky Mountains. Beside from The Rocky Mountains diagnosis, we wish to employ our model to solve for balanced fields with isentropes intersected with ground.

Tibetan plateau affects nearby climatology significantly. It penetrates to about 600 hPa, which can heat the atmosphere directly through sensible heat. The ERA5 reanalysis data in July, 2020 is shown in Figure 31. One of the most prominent LLJs in north hemisphere warm season is the Somali jet, a southwesterly jet stream that provides sufficient moisture for south Asia in Monsoon season. Although the maximum wind speed of the Somali jet is at about 850 hPa, we can identify the jet stream in 700 hPa observed fields.

The 3-D numerical simulation was performed and the horizontal fields at 700 hPa are shown in Figure 32. The overall patterns are captured by our model, including the Somali jet, the warmer region in West Asia, and the weak southerly in the east of the Tibetan plateau. The horizontal profile of observation and the numerical result are shown in Figure 33 and Figure 34. In observation, the maximum wind speed of the Somali jet is up to 15 m/s, while the wind speed is about 10 m/s (Figure 33), Beside, the return flow and slightly heated surface at the

southern part of the plateau in Figure 33 (b) doesn't appear in observed field; Furthermore, the model overestimated southerly at the east of the Tibetan plateau in Figure 34. Both inconsistencies are accompanied with opposing heating or cooling thermal fields near the topography. Such inconsistency occurs may remind us of the importance of properly choosing of massless layer profile.

Additionally, we focused on how strong south-westerly interacts with Taiwan island. A 24 hour averaged reanalysis data on 20 July 2015 shows that a northeast-southwest-oriented PV band near the southwestern coast of China, inducing south-westerly flow at its right-hand side, as shown in Figure 35 (a). This PV band structure vertically extended to roughly 300 hPa, as shown in Figure 36.

The zonal profiles across Taiwan island in observations and numerical results are shown in Figure 37. Balanced model can capture the vertical extension of strong southerly induced by the PV band. The wind speed of south-westerly is about 19.2 m/s between 800hPa and 600 hPa in observations and balanced models can produce wind speed up to 16.5 m/s. The difference between them is about 16%, which might result from the existence of transient fields, which would disappear after the geostrophic adjustment process. Besides, in observations, the stream right above topography is weak, such feature can be captured by balanced model. However, small scale temperature gradient on the Taiwan island is not captured by model, which indicates that in horizontal scale around 100 km is too small for geostrophic adjustment process. In summary, the wind and thermal fields patterns in the model are overall consistent with observation.

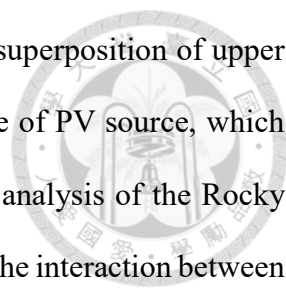
CHAPTER 5

Conclusions



We emphasized the importance of PV dynamics again in this article, especially in the invertibility principle. We focused on previous studies about the practical and theoretical developments of the PV invertibility principle. With the progress of computational ability, some nonhydrostatic, full-physics models like WRF and CReSS are widely used in investigating complex and nonlinear interactions between moist process and dynamics. However, the research on balanced dynamics is still worthwhile since that the moist and complicated thermal dynamics could produce balanced dynamics and the resultant balanced dynamics could feedback to thermal dynamics. More clear physics could be shown in balanced models in topics such as dynamical efficiency, PV mixing, and center pressure fall in the eyewall in the typhoon rapid intensification processes (Tsuji no and Kuo 2020). In the whole rapid intensification procedure, balanced dynamics play an important role in .

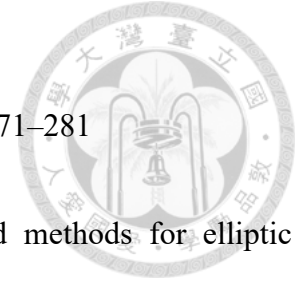
We mainly followed the concept of model construction from Silvers and Schubert (2012) and Fulton et al. (2017). We have built balanced model, and studied the idealized numerical simulations in 2-D and 3-D geometries. The dynamics of LLJs in Silvers and Schubert (2012) are reproduced and further gave a quantitative analysis of the effect from both thermal and orographic forcing. The wind field forcing could be represented as the linear combination of both surface thermal forcing and topography effect, which fits the geostrophic-balanced invertibility principle. With a Gaussian-shaped mountain, we further show the LLJs structure would be spoiled if there is an idealized inversion layer below the height of the ridge. On the other hand, if the inversion layer is set above the height of the ridge, the cyclonic flow would be enhanced. For a 3-D invertibility, we found that the flow strength of the LLJs would be weaker than a 2-D case. We also perform PV inversion near The Rocky Mountains in warm season. The results bear much resemblance to features in observations, especially in 3-D



numerical results with a 50 hPa massless layer lifting adjustment. The superposition of upper and lower dynamics wind fields implies that we can trace the influence of PV source, which manifests the importance of PV invertibility principle. Aside from the analysis of the Rocky Mountains, we diagnosed the ambient flow of Tibetan plateau as well as the interaction between the southwesterly flow and the Taiwan island. In the PV inversion of the Tibetan plateau, the flow and thermal patterns that are partially captured by the model. The wind deviated from observed fields might be corrected by drawing better lower boundary condition. In the PV inversion of the Taiwan island, the wind induced by PV band in the balanced model is the same order with observed fields, which reminds us that the balanced dynamics can account for most of the observed fields in daily time-scale. The smoothness of low-level wind is also consistent with the PV invertibility dynamics.

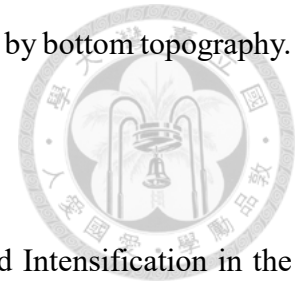
In summary, our works include: 1) reviewing PV dynamics, especially the PV invertibility dynamics 2) building 3-D linear and nonlinear balanced models with massless layer approach, 3) simulating and analyzing several idealized PV inversion experiments, 4) simulating and analyzing real case PV inversions based on ERA5 reanalysis data, and 5) developing an interpolation method to solve elliptic partial differential equations easily and effectively.

Bibliography



- Ertel, H, 1942: Ein Neuer hydrodynamischer Wirbelsatz. *Met. Z.*, **59**, 271–281
- Fulton, S.R., Ciesielski, P.E. and Schubert, W.H., 1986: Multi-grid methods for elliptic problems: a review. *Mon. Wea. Rev.*, **114**, 943–959.
- Fulton, S. R., W. H. Schubert, and S. A. Hausman, 1995: Dynamical adjustment of mesoscale convective anvils. *Mon. Wea. Rev.*, **123**, 3215–3226.
- Fulton, S. R., Schubert, W. H., Chen, Z. & Ciesielski, P. E. 2017: A dynamical explanation of the topographically bound easterly low-level jet surrounding Antarctica. *J. Geophysical Research: Atmospheres*, **122**, 12,635–12,652.
- Galimore, R. G. and D. R. Johnson 1981: The forcing of the meridional circulation of the isentropic zonally average circumpolar vortex, *J. Atmos. Sci.*, **38**, 583-599.
- Guinn, T. A., and W. H. Schubert, 1993: Hurricane spiral bands. *J. Atmos. Sci.*, **50**, 3380–3403.
- , and ——, 1994: Reply. *J. Atmos. Sci.*, **51**, 3545–3546
- Hoskins, B. J., 1982: The mathematical theory of frontogenesis. *Annu. Rev. Fluid Mech.*, **14**, 131–151.
- Hoskins, B. J., M. E. McIntyre, and A. W. Robertson, 1985: On the use and significance of isentropic potential vorticity maps, *Q. J. Meteorol.*, **111**, 877-946.
- Hoskins, B. J., 2015: Potential vorticity and the PV perspective. *Adv. Atmos. Sci.*, **32**, 2–9

Eliassen, A. 1980. Balanced motion of a stratified, rotating fluid induced by bottom topography. *Tellus* **32**, 537–547.



S. Tsujino, and H. C., Kuo 2020: Potential Vorticity Mixing and Rapid Intensification in the Numerically Simulated Supertyphoon Haiyan (2013), *J. Atmos. Sci.*, **77**, 2067–2090.

Schubert, W. H., and B. T. Alworth, 1987: Evolution of potential vorticity in tropical cyclones. *Quart. J. Roy. Meteor. Soc.*, **113**, 147–162.

Schubert, W. H., P. E. Ciesielski, C. Lu, and R. H. Johnson, 1995: Dynamical adjustment of the trade wind inversion layer. *J. Atmos. Sci.*, **52**, 2941–2952.

Silvers, L. G., and W. H. Schubert (2012), A theory of topographically bound balanced motions and application to atmospheric low-level jets, *J. Atmos. Sci.*, **69**, 2878–2891.

Vera, C., et al. (2006), The South American Low -Level Jet Experiment, *Bull. Am. Meteorol. Soc.*, **87**, 63–77,

Fulton SR, Ciesielski PE, Schubert WH. 1986. Multigrid methods for elliptic problems – a review. *Mon. Weather Rev.* **114**: 943–959.

Appendix



A. Model Discretization

With the reference state, we can rewrite (35) into

$$\alpha \left(f + \frac{\partial^2 \psi}{\partial x^2} \right) + f \frac{\partial^2 \psi}{\partial \theta^2} = \frac{\tilde{\sigma}}{\theta \rho P} \quad (\text{A.1})$$

We define $(x_i, \theta_j) = (x_1 + i\Delta x, \theta_j + j\Delta\theta)$ with $i = 1, 2, \dots, m$ and $j = 1, 2, \dots, n$ in the domain. They represent the horizontal and vertical grid points, respectively. Therefore, we have discretized function $f_{i,j}$ that corresponds to $f(x_i, \theta_j)$.

Hence, (A.1) can discretize into

$$\alpha_{i,j} \left(\frac{\psi_{i+1,j} + \psi_{i-1,j} - 2\psi_{i,j}}{\Delta x^2} \right) + f \left(\frac{\psi_{i,j+1} + \psi_{i,j-1} - 2\psi_{i,j}}{\Delta \theta^2} \right) = F_{i,j} \quad (\text{A.2})$$

, where

$$F_{i,j} = \frac{\tilde{\sigma}_{i,j}}{\theta_j \tilde{\rho}_{i,j}} - \alpha_{i,j} f \quad (\text{A.3})$$

and

$$\begin{cases} \alpha_{i,j} = \frac{g}{\theta_j \rho_{i,j} P_{i,j}} & , \text{when } \theta \geq \theta_s \quad - \\ 0 & , \text{when } \theta < \theta_s \quad - \end{cases} \quad (\text{A.4})$$

Note that $\rho_{i,j}$ is a function of $\psi_{i,j}$.

For vertical pressure

$$\begin{aligned} \Pi_{i,j} = \tilde{\Pi}_j + f \left(\frac{\psi_{i,j+1} - \psi_{i,j-1}}{2\Delta\theta} \right) & , \text{when } \theta \geq \theta_s \quad - \\ & , \text{when } \theta < \theta_s \quad - \end{aligned} \quad (\text{A.5})$$

, where $\tilde{\Pi}_j = \tilde{\Pi}(\theta_j)$ is the reference state.

The upper boundary is determined by

$$\psi_{i,n+1} = \psi_{i,n-1} + 2\Delta\theta [\Pi_{i,n} - \tilde{\Pi}(\theta_n)] \quad (\text{A.6})$$

and the lower boundary conditions is described by

$$\psi_{i,0} = \psi_{i,2} + \frac{2\Delta\theta}{\theta_B} \left[\psi_{i,1} - \frac{\Phi_S(x_i)}{f} \right] \quad (\text{A.7})$$

Although in most of the situations the density deviation from the reference state is small, it is still a function of ψ and can be written down as

$$\rho_{i,j} = \frac{p_0}{R_d \kappa} \left(\frac{\Pi_{i,j}}{c_p} \right)^{\frac{c_p - 1}{R_d}} \quad (\text{A.8})$$

, where $\Pi_{i,n}$ is unknown. Therefore, iterative technique is necessary to solve for both $\psi_{i,j}$ and corresponding $\alpha_{i,j}$. To make the model converge, we need to do iterations in different loops. In the inner loop, the model did several times iteration for (A.2) and (A.3), applied all boundary conditions, (A.5), and (A.7) the density as a function of Π . Then, the residual of equation (A.2) was calculated. In the model we used, 20 times iteration is used in the inner loop. In the outer loop, the model repeated the inner loop except that the residual of (A.2) was below the criteria. The way we chose the criteria would be mentioned in next section. Additionally, to speed up the convergence rate, we applied interpolation method, which would be introduced in next section as well.

Besides, from Figure A. we know that the criteria are small enough for both the wind fields difference in 2-D models ($\Delta u < 0.1$ m/s) and in 3-D models ($\Delta u < 1$ m/s).

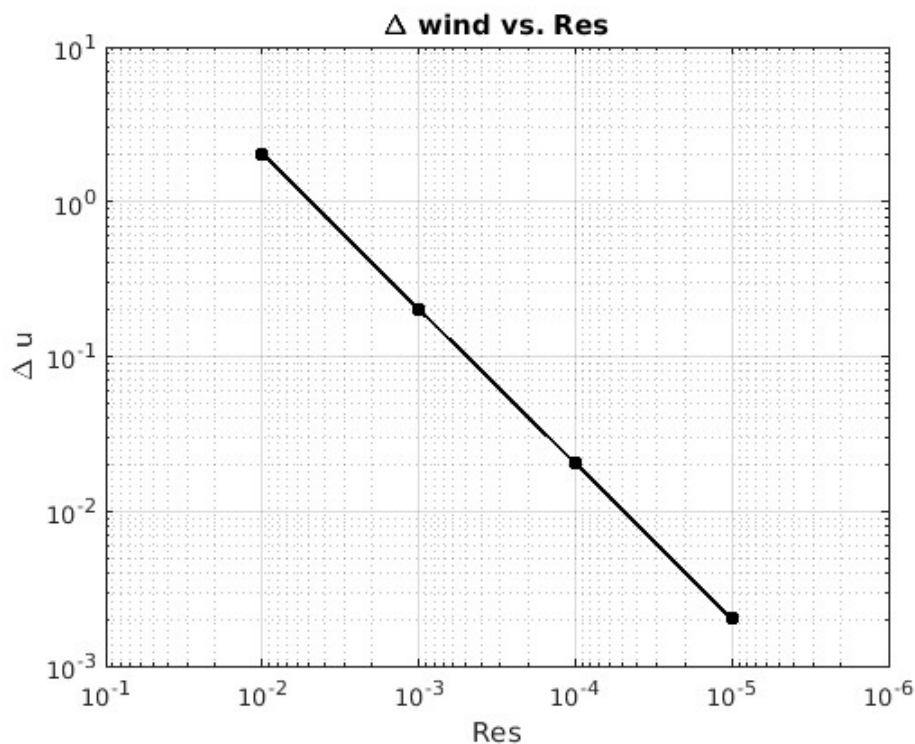
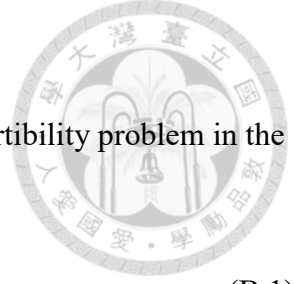


Figure A.1. The wind difference for Fig 8 as residual decrease. (e.g. abscissa RES = 10^{-2} means that the u_{\max} which residual is equal to 10^{-2} minus the u_{\max} which residual is equal to 10^{-1}).

Table 2. The model resolutions and the residual as criteria for the convergence of models

	2-D		3-D			
	2-D idealized exp.	Rocky Mountains	Rocky Mountains	Tibetan Plateau	Taiwan	Nonlinear
Resolutions (grid number)	(511, 2047)		(255,63,127)	(181,91,127)	(91,91,127)	(31,31,20)
Residual to converge	1×10^{-4}		1×10^{-2}			



B. Model Convergence rate Experiments

We start from solving Poisson's equation, which served as an invertibility problem in the simplest version

$$\nabla^2 \psi = \zeta \quad (\text{B.1})$$

and the boundary conditions apply

$$\psi = 0 \quad \begin{array}{l} , \text{ at } x = \pm L_x \\ , \text{ at } y = \pm L_y \end{array} \quad (\text{B.2})$$

Discretize and rearrange (B.1), we obtain

$$\psi_{i,j} = \frac{1}{4} \left(\psi_{i+1,j} + \psi_{i-1,j} + \psi_{i,j+1} + \psi_{i,j-1} - \frac{\zeta_{i,j}}{h^2} \right) \quad (\text{B.3})$$

Jacobi's iterative method is suitable for solving such linear algebra manipulation due to vectorization techniques in MATLAB or python. With this method, we have $n + 1$ step based on n step:

$$\phi_{i,j}^{n+1} = \frac{1}{4} \left(\phi_{i+1,j}^n + \phi_{i-1,j}^n + \phi_{i,j+1}^n + \phi_{i,j-1}^n - \frac{\zeta_{i,j}}{h^2} \right) \quad (\text{B.4})$$

Taking the difference between (B.3) and (B.4), we obtain

$$e_{i,j} = \frac{1}{4} (e_{i+1,j} + e_{i-1,j} + e_{i,j+1} + e_{i,j-1}) \quad (\text{B.5})$$

, which indicates that in relaxation method every iteration is just performing error smoothing procedure. If the error distribution is smooth, then according to (B.2), the error can only be eliminated by the boundary conditions. Course grid points in the model let error decrease faster than fine grid points since we need fewer iteration step to dissipate the error in the center of the domain. On the other hand, high wave number error can also be dissipated quickly through error smoothing, as shown in Figure B.. In other words, both lower resolution and small low wave number error are the keys to make models converge fast.

The traditional multigrid method involved residual transfer, which means that the variables and their residuals would be transferred from finer grid to courser grid. (see Fig. 4 in Fulton et al. 1986). Multigrid methods are very efficient in solving elliptic partial differential

equations. However, multigrid methods are usually complicated and might be not suitable for solving partial differential equations that possess nonhomogeneous coefficients. Furthermore, due to vectorization techniques in MATLAB or python, extra rearrangement procedures in multigrid methods would spend much time. Therefore, we turned to develop an interpolation method to reduce model runtime. Interpolation method is to solve course grid relaxation to obtain a solution first. Then simply apply this solution as an initial guess by interpolation.

We give elliptical Rankine vortex vorticity and solve streamline. The given vorticity and the numerical result streamline are all shown in Figure B.. Note that the solution shows the property that the solution for Poisson's equation, as an elliptical equation, is smooth and less sharp than its source. We solve for this problem in three methods: Jacobi iterative method, multigrid method, and interpolation method, and their converging rates are shown in Figure B.. We found that the multigrid method is still efficient in solving the homogeneous coefficient equation like (B.3). The interpolation method can quickly dissipate high wave number error, but the error decreasing rate is slow down and approaches the rate of Jacobi iterative method after 250 seconds, which indicates the dominate of the low wave number error.

In summary, based on Jacobi iterative method, we developed an interpolation method, which can be as a "simplified" multigrid method that lets our models converge quickly.

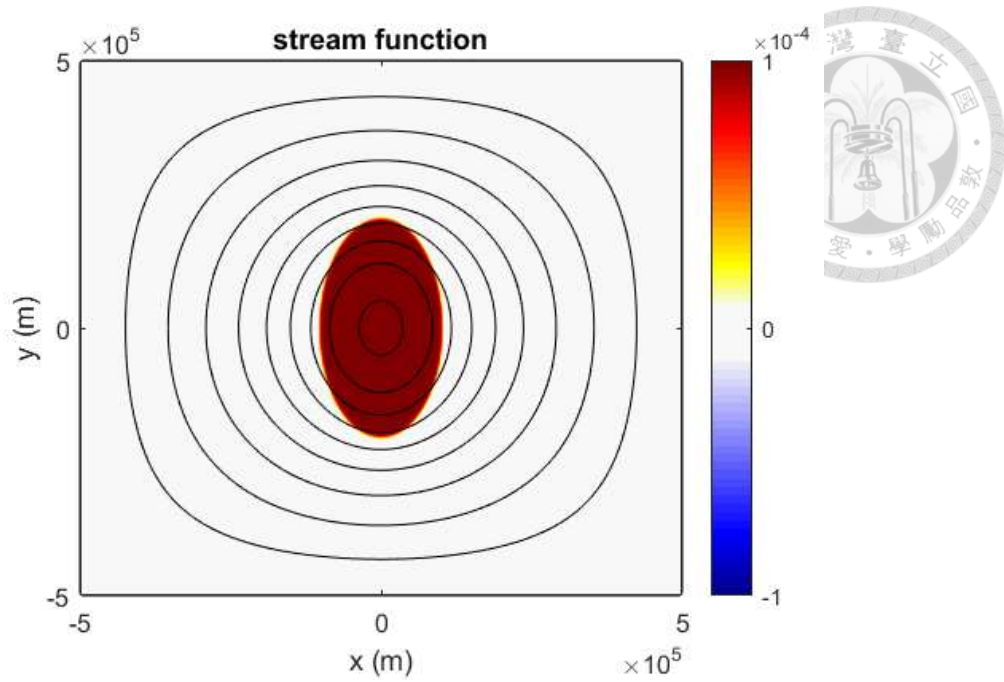


Figure B.1. The vorticity (shading, in 1/s) and the streamfunction (contour).

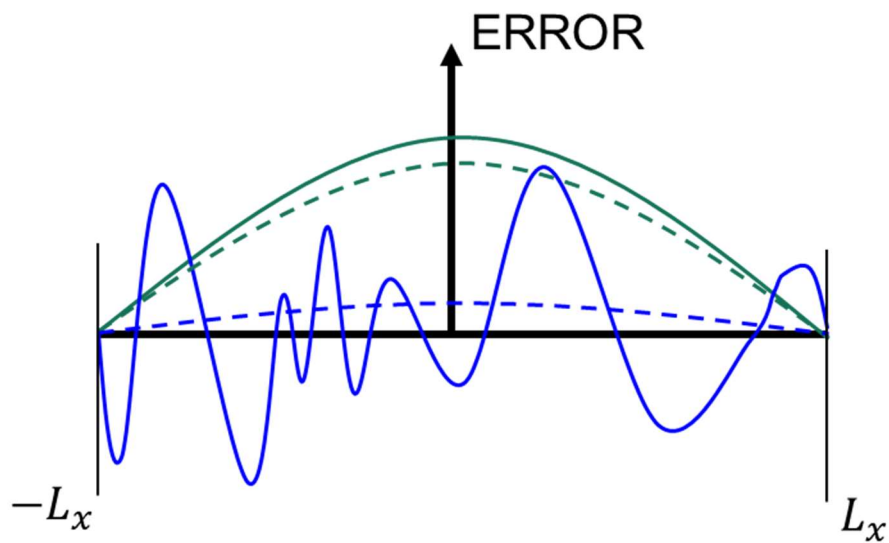


Figure B.2. Schematic diagram for error smoothing (relaxation) processes. It is shown that after several error smoothing procedures, the initial low wave number error (in green solid line) decrease slowly (in green dashed line). However, initial high wave number error (in blue solid line) dissipates quickly (in blue dashed line).

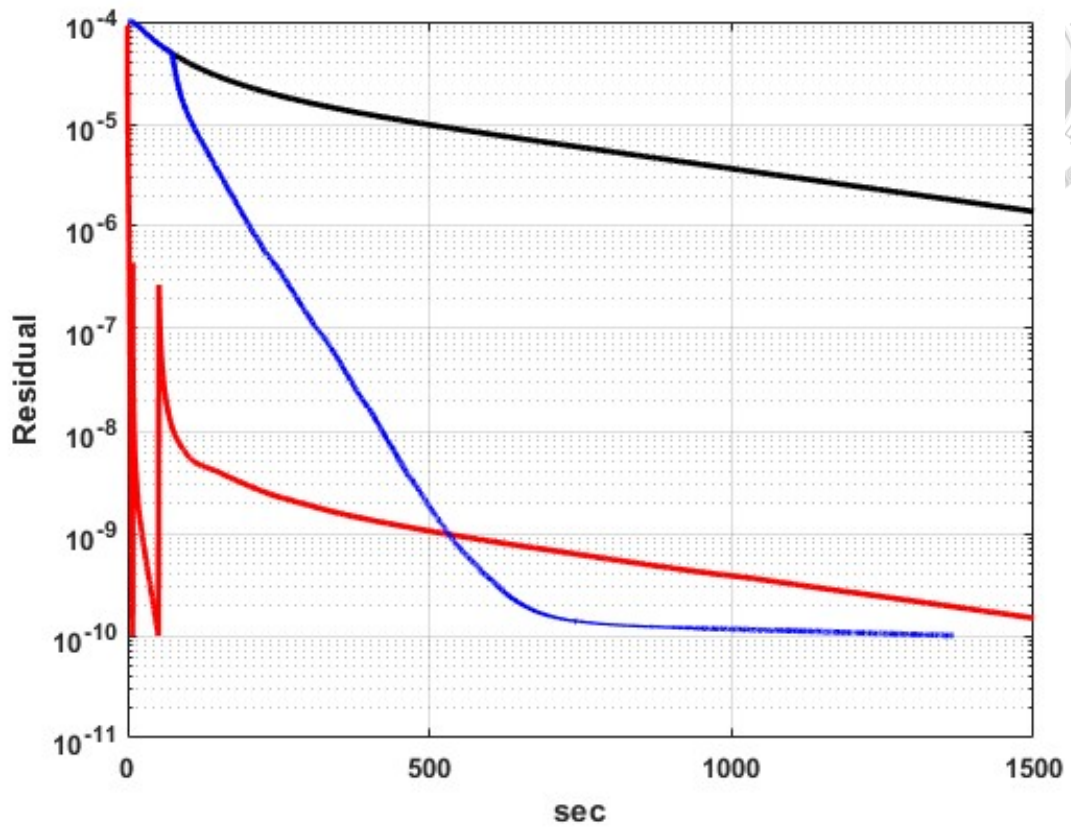


Figure B.3. Residual versus model run time. Black, blue, and red line represent Jacobi iterative method, multigrid method (see Fulton et al. 1986), and interpolation method, respectively.

C. Nonlinear Balance Model Solution

In nonlinear balance relation

$$\nabla^2 M = f \nabla^2 \psi + 2J(\psi_x, \psi_y) \quad (C. 1)$$

We can obtain invertibility principle with M only, like (28). We need to solve both M and ψ at the same time. The strategy we used to solve nonlinear balance invertibility problem is we solve M in (C. 2) mainly. Replace (C. 1) into (23), we obtain

$$\begin{cases} \frac{g}{\theta \rho P} \left\{ f + \frac{1}{f} [\nabla^2 M - 2J(\psi_x, \psi_y)] \right\} + \frac{\partial^2 M}{\partial \theta^2} = 0 & , \text{when } \theta \geq \theta_s \quad - \\ \frac{\partial^2 M}{\partial \theta^2} = 0 & , \text{when } \theta < \theta_s \quad - \end{cases} \quad (C. 2)$$

Iteration method was used to solve this invertibility problem. We solve for ψ with (C. 1), and solve for M with (C. 2). Note that both equations need to perform relaxation. In case that when Jacobian term is smaller than linear term, the solution can be easily obtained using interpolation method. However, in typhoon-like case, the order of magnitude of Jacobian term can be dominated in (C. 1) and therefore the model may not converge. In such a situation, we applied several ways to make the model converge. For example, method of continuity, underrelaxation method, and lower vertical resolution. Method of continuity is a way that we add up the forcing gradually in relaxation procedures to prevent our initial guess deviating from the end solution too much. For example, in typhoon-like case we added 3 PVU on the magnitude of PV at once and performed relaxation until 20 PVU was reached. Similarly, underrelaxation can slow down the relaxation procedures to prevent singularity point occurs. However, somehow higher vertical resolution still makes the model diverge anyway. Therefore, in Figure 18 we adjusted the vertical grid number and finally the nonlinear balanced models can produce typhoon-like cases.

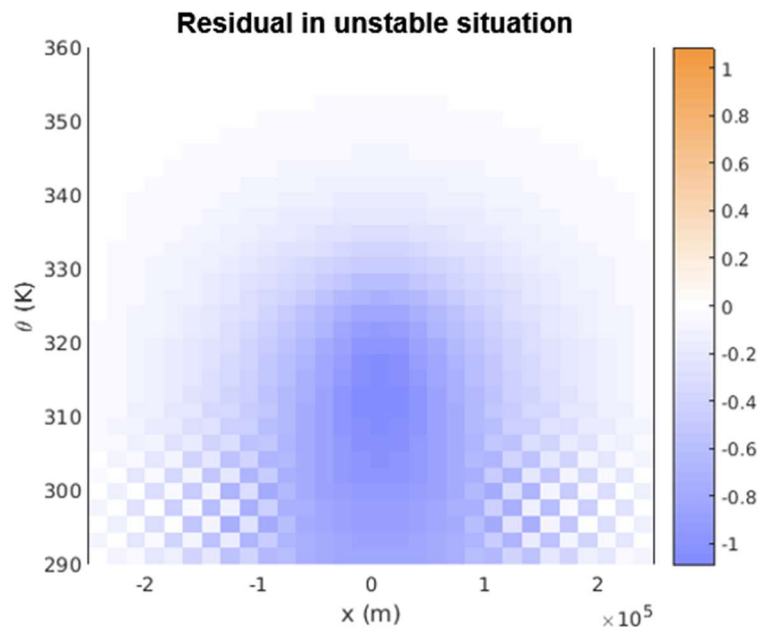


Figure C.1. A snapshot for unstable relaxation case. In nonlinear Jacobian term dominating situations, the relaxation method may somehow result in the error smoothing process fails and the model diverge.

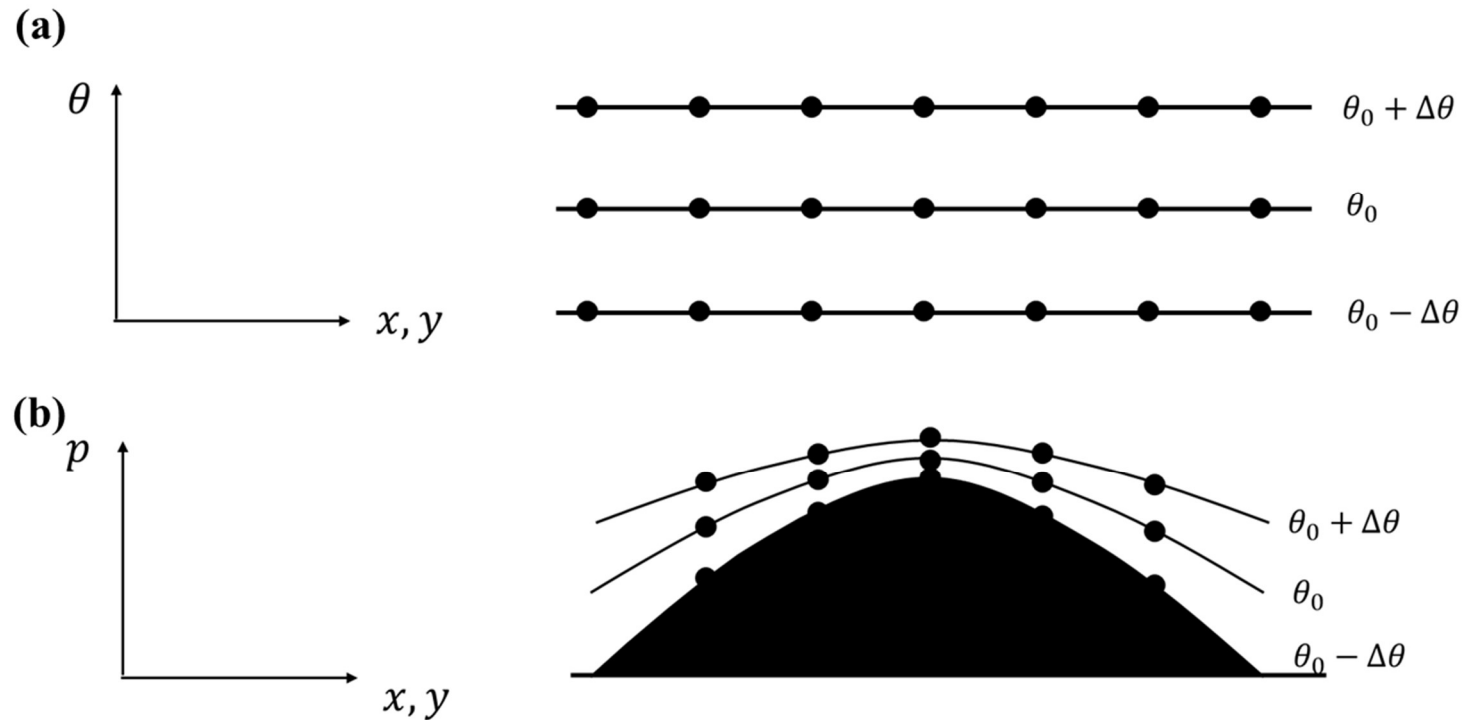


Figure 1. The schematic diagram for how topography boundary conditions change isentropes in isobaric and isentropic coordinates. (a) Uniform grids on isentropic coordinate. The topography is invisible if we focus on the isentropes. (b) In pressure coordinate, isentropes bend upward due to topography (cooling effect).

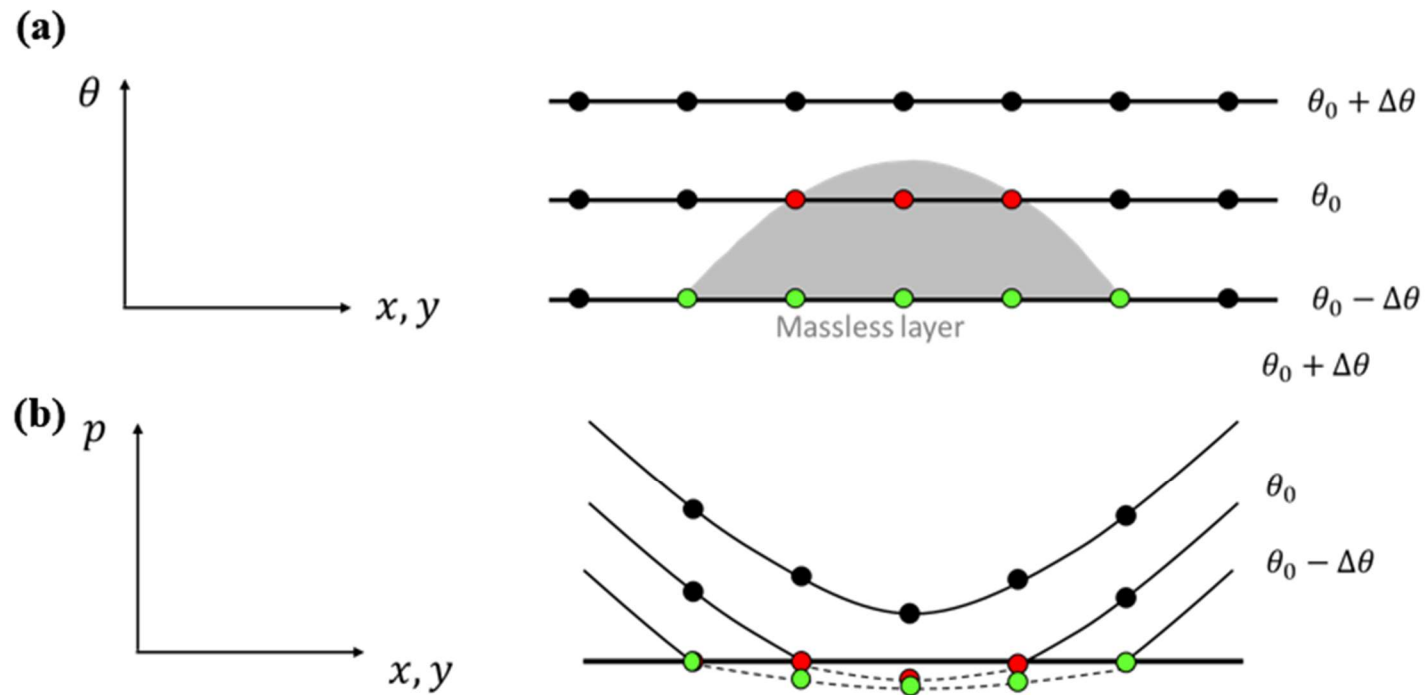
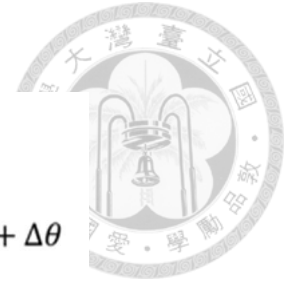


Figure 2. The schematic diagram for how isentropes intersect with ground in isobaric and isentropic coordinates. (a) Uniform grids on isentropic coordinate. The grey shaded region is massless layer. (b) In pressure coordinate, isentropes bend downward due to surface temperature anomaly

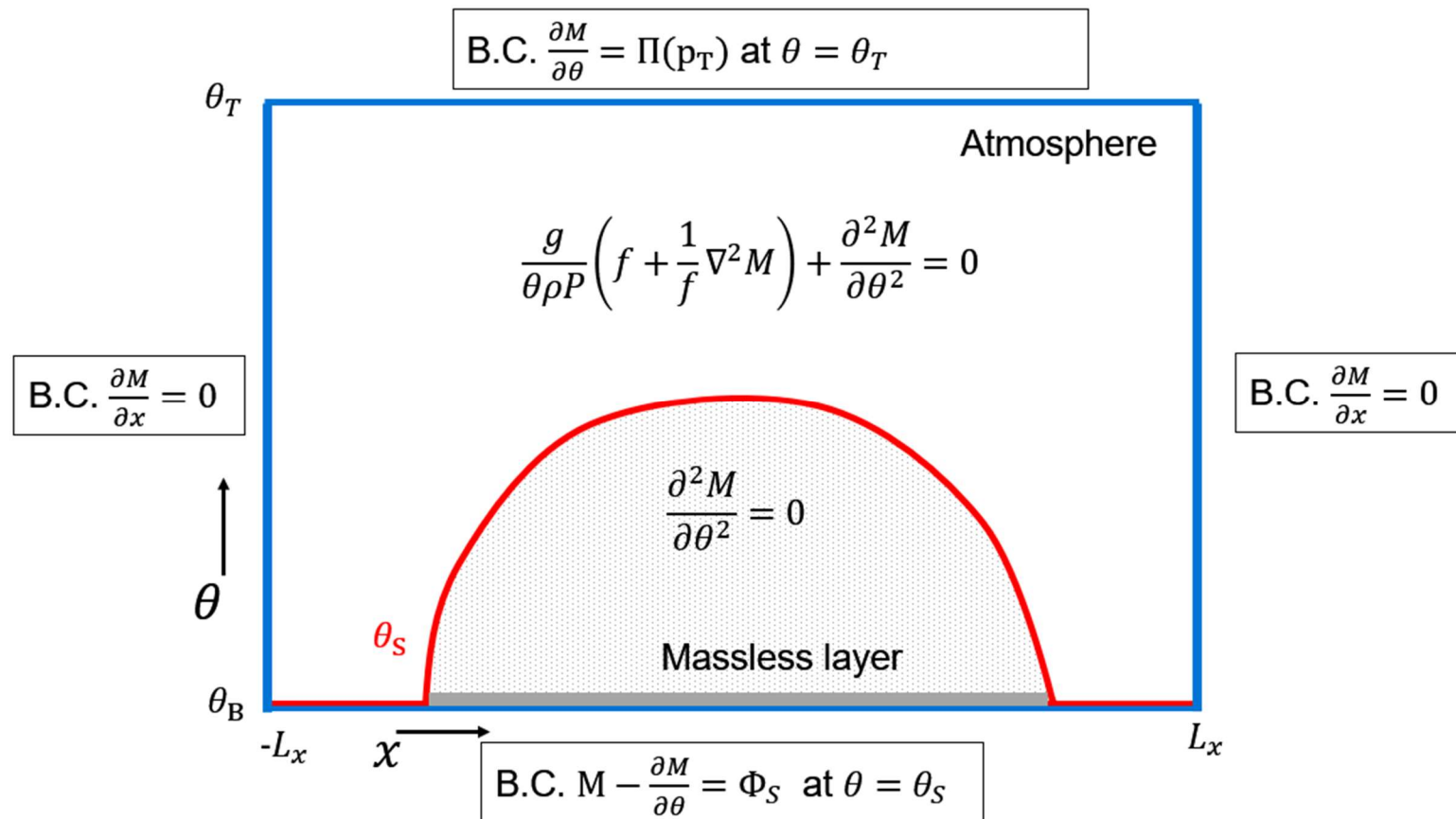


Figure 3. The schematic diagram for the isentropic model. The governing equations and the boundary conditions are shown. The gray shaded region represents massless layer area which different governing equation is applied.

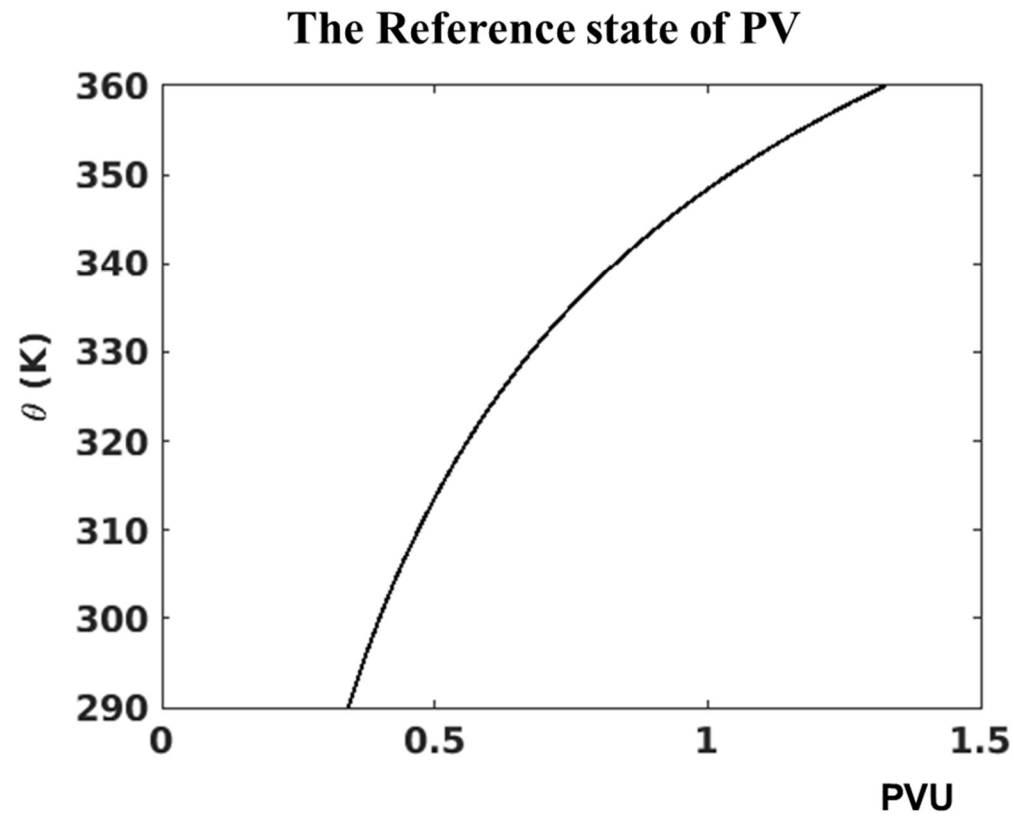


Figure 4. The reference state of PV field as a function of θ , computed from (34). The Coriolis coefficient is set as $f = 7.3 \times 10^{-5} \cong 2\Omega \sin(30^\circ)$.

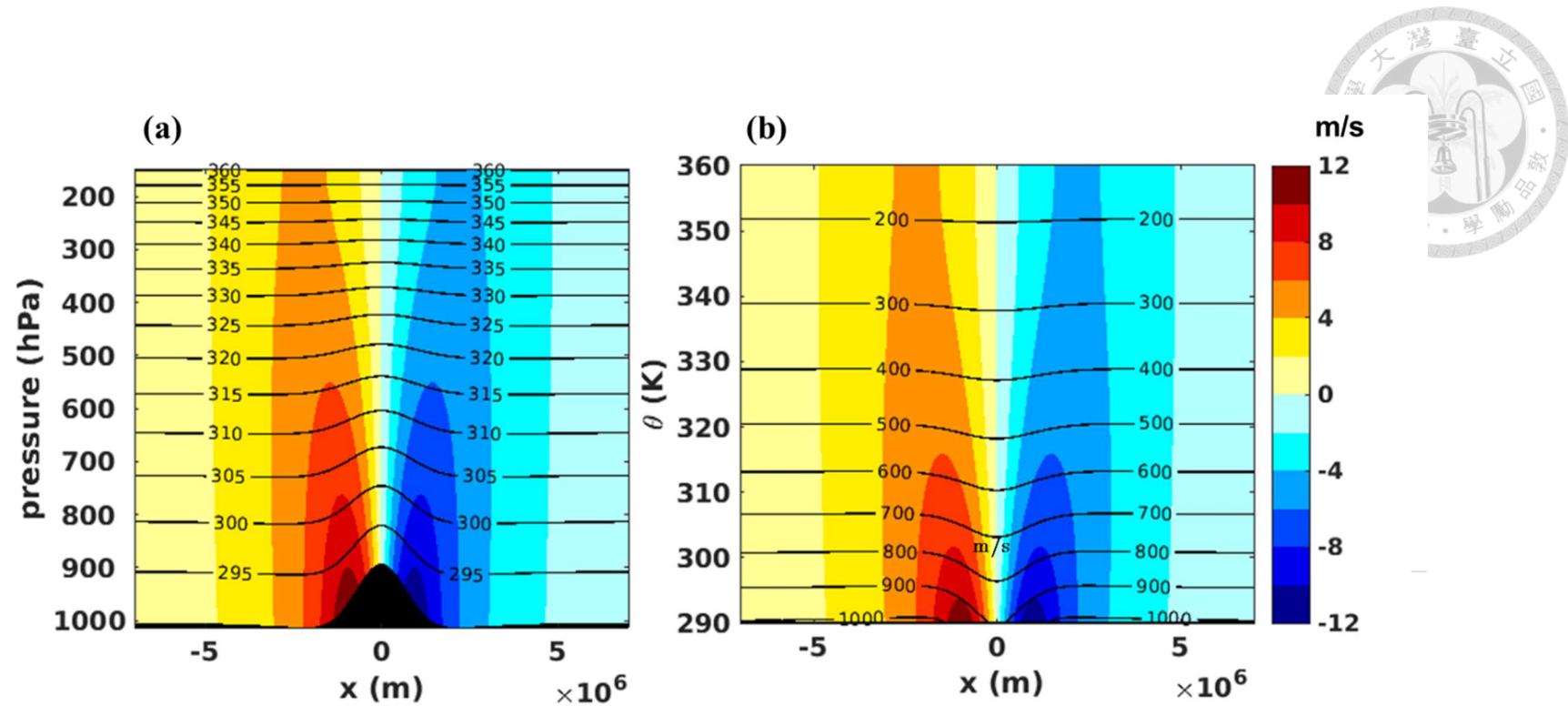


Figure 5. Meridional wind field (shading) in (a) isobaric coordinate with θ (contour, in K) and (b) isentropic coordinate with pressure (contour, in hPa) under the effect of topography $\Phi_0 = 1200$ km. The LLJs are with anti-symmetric and anti-cyclonic patterns near the mountain, with maximum anticyclonic flow up to 11.3 m/s.

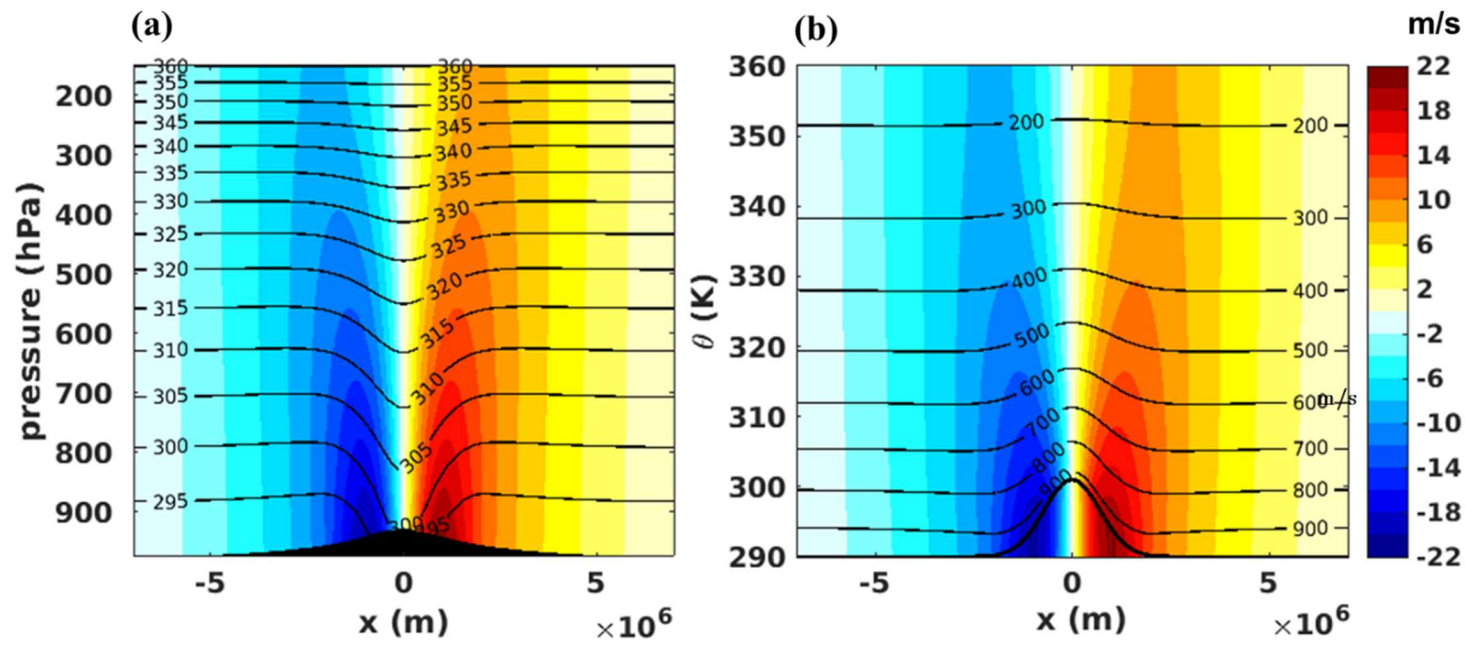


Figure 6. As in Figure 5, but with surface temperature anomaly instead of topography. Near the thermal forcing region, the cyclonic flow is induced with wind speed up to 20.4 m/s.

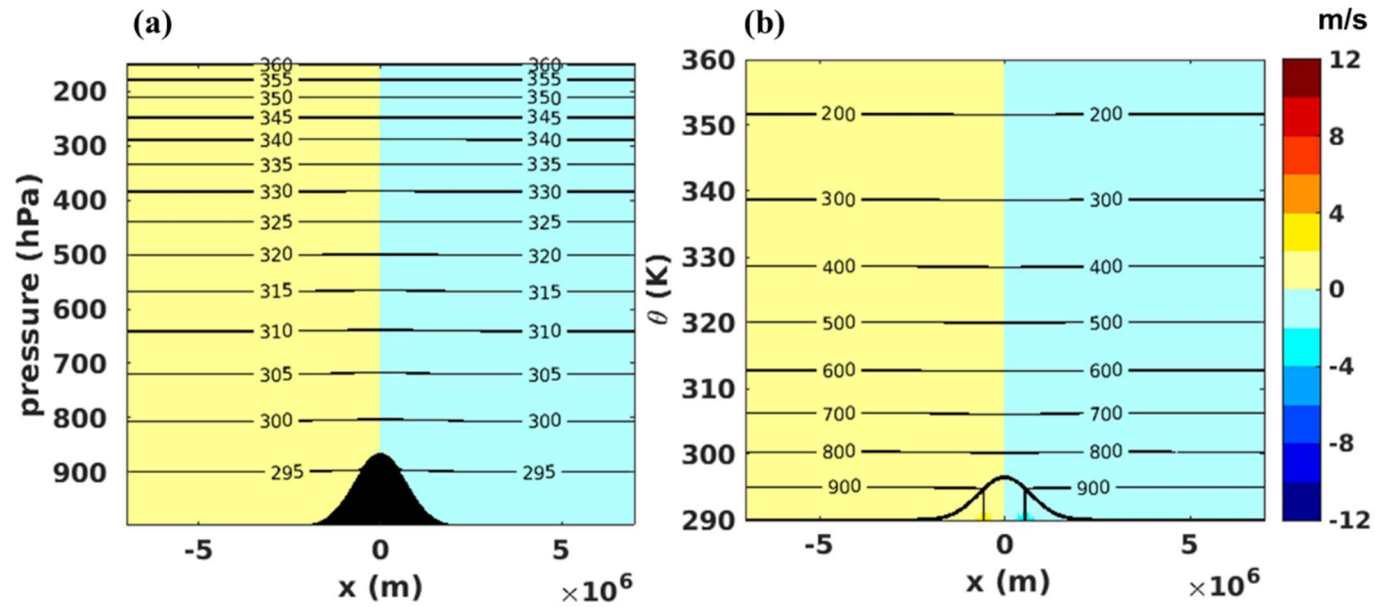


Figure 7. As in Figure 5, but with both surface heating $\theta_0 = 6.5$ K and topography $\Phi_0 = 1200$ km. There is nearly no wind in physical domain. The maximum value $v = 0.69$ m/s.

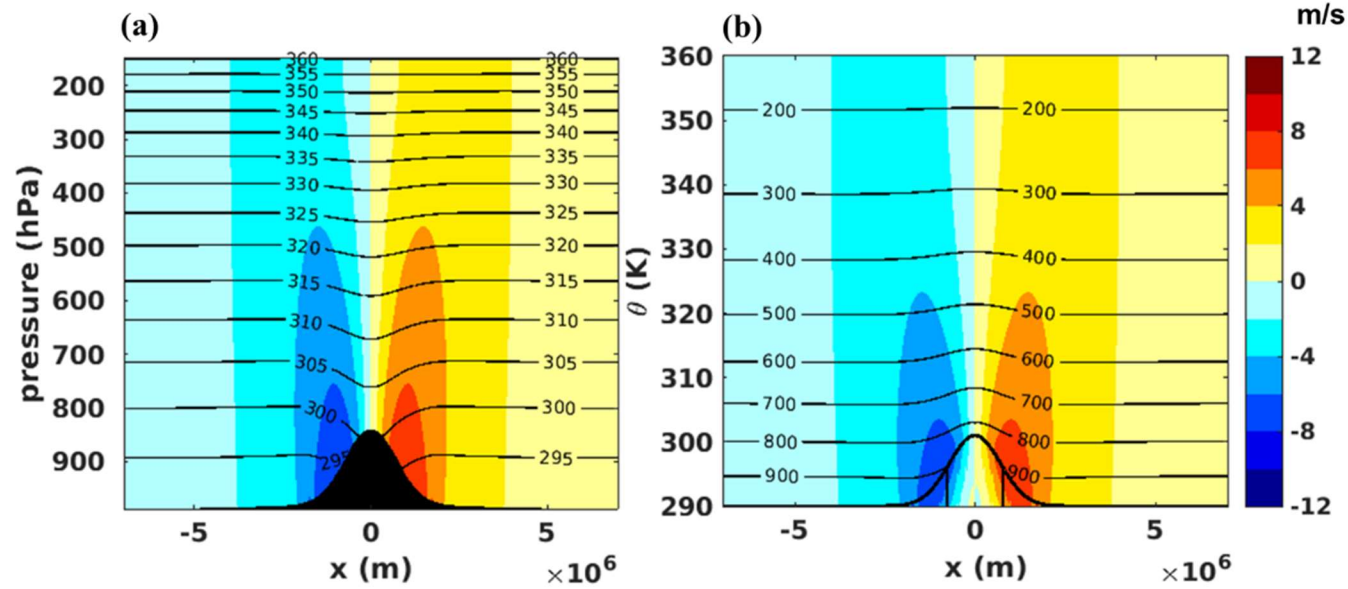


Figure 8. As in Figure 5, but with both surface heating $\theta_0 = 11$ K and topography $\Phi_0 = 1200$ km. The low-level jets have anti-symmetric and cyclonic patterns near the heating mountain, with maximum value $v = 8.0$ m/s.

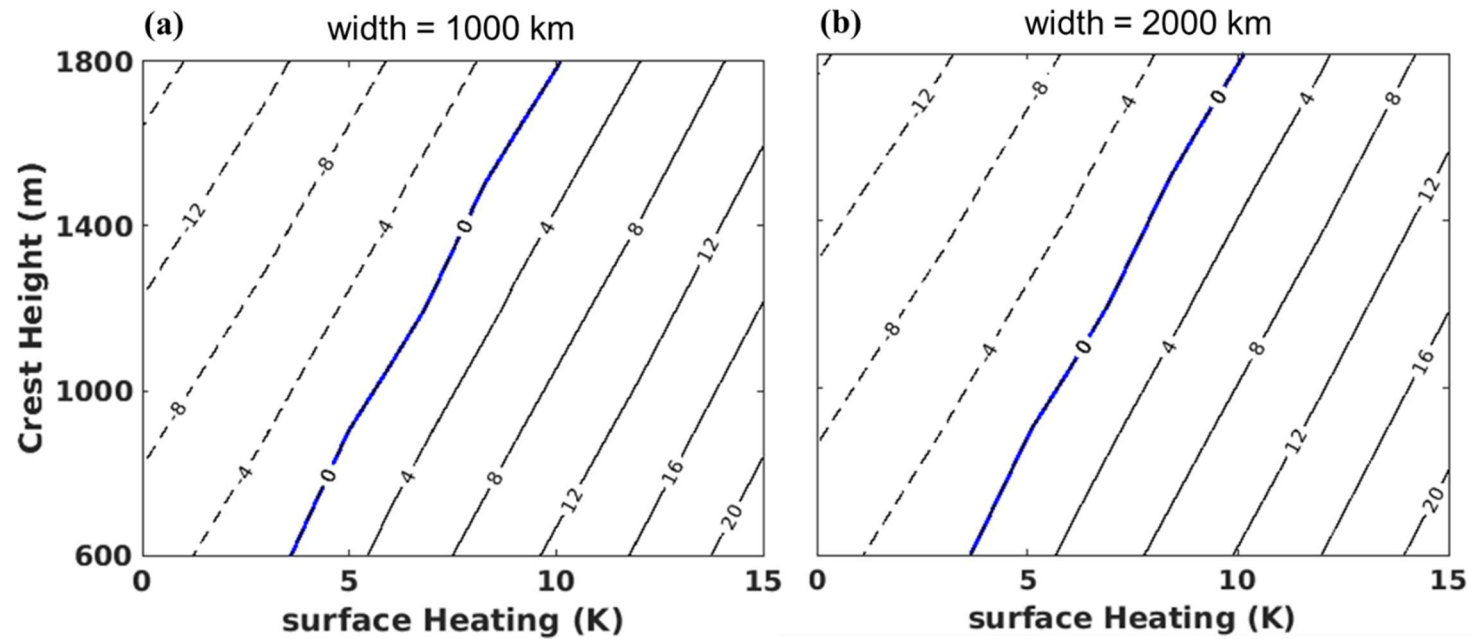


Figure 9. The relation between Gaussian-Shaped topographic forcing and surface thermal forcing. (a) width = 1000 km, $v_{max} = 0.1 + 1.9\Delta T - 0.01\Delta H$, with $R^2 = 0.9984$ (b) width = 2000 km, $v_{max} = 0.1 + 1.8\Delta T - 0.01\Delta H$, with $R^2 = 0.9969$. The forcing effects are quite linear and nearly independent of the width of the mountain.

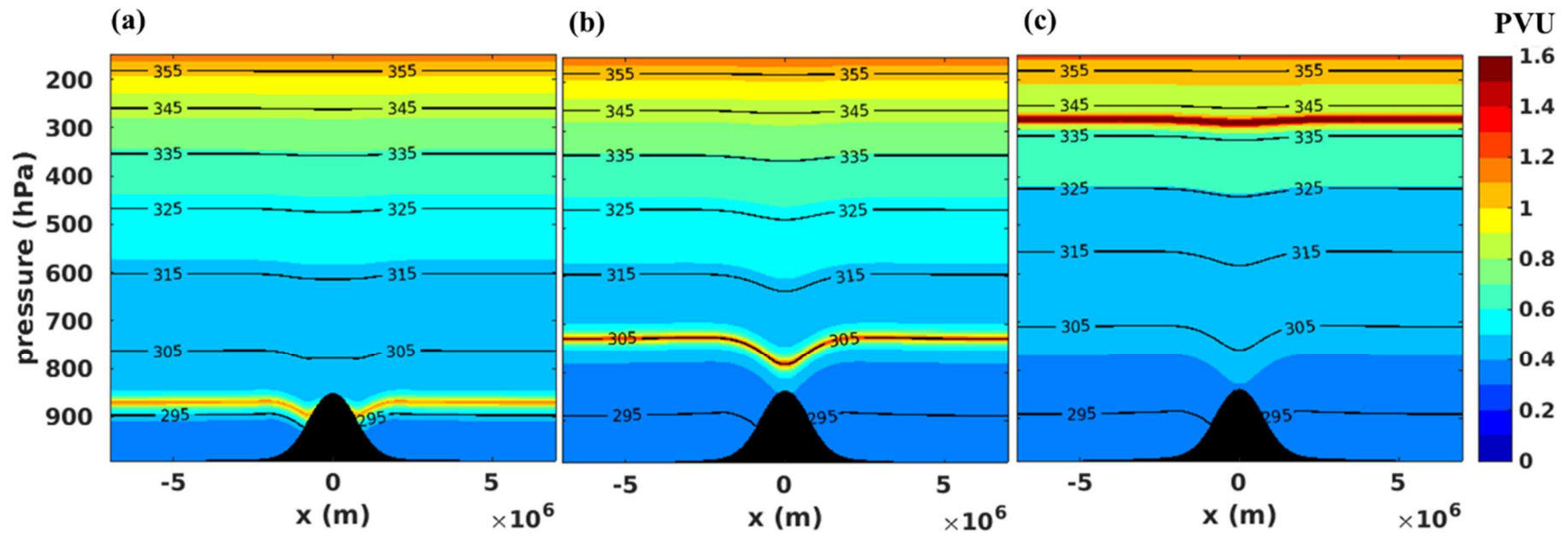


Figure 10. PV anomaly as inversion layer (shading, in PVU) and isentropes (contour, in K) in pressure coordinate. Inversion layers locate in (a) 297.5 K (b) 305 K (c) 340 K.

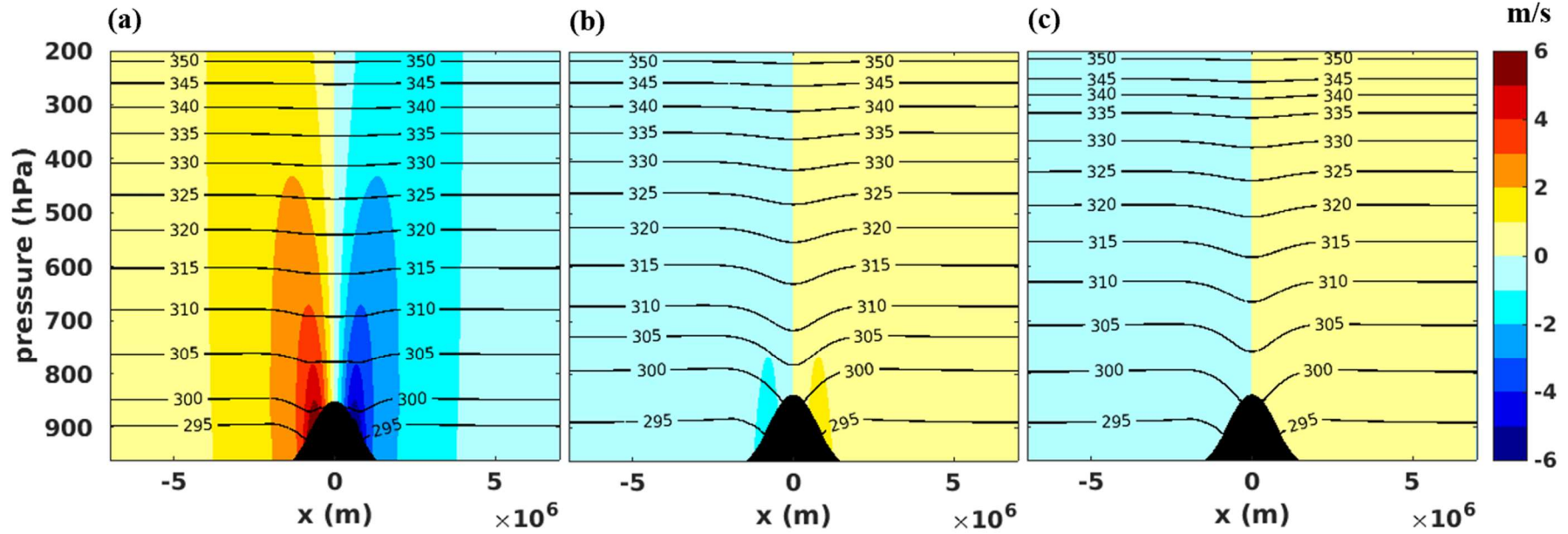
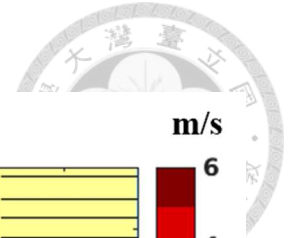


Figure 11. Wind difference from Figure 8 (a) due to the existence of inversion layer (shading, in m/s) and isentropes (contour, in K) in pressure coordinate. Inversion layers locate in (a) 297.5 K (b) 305 K (c) 340 K.

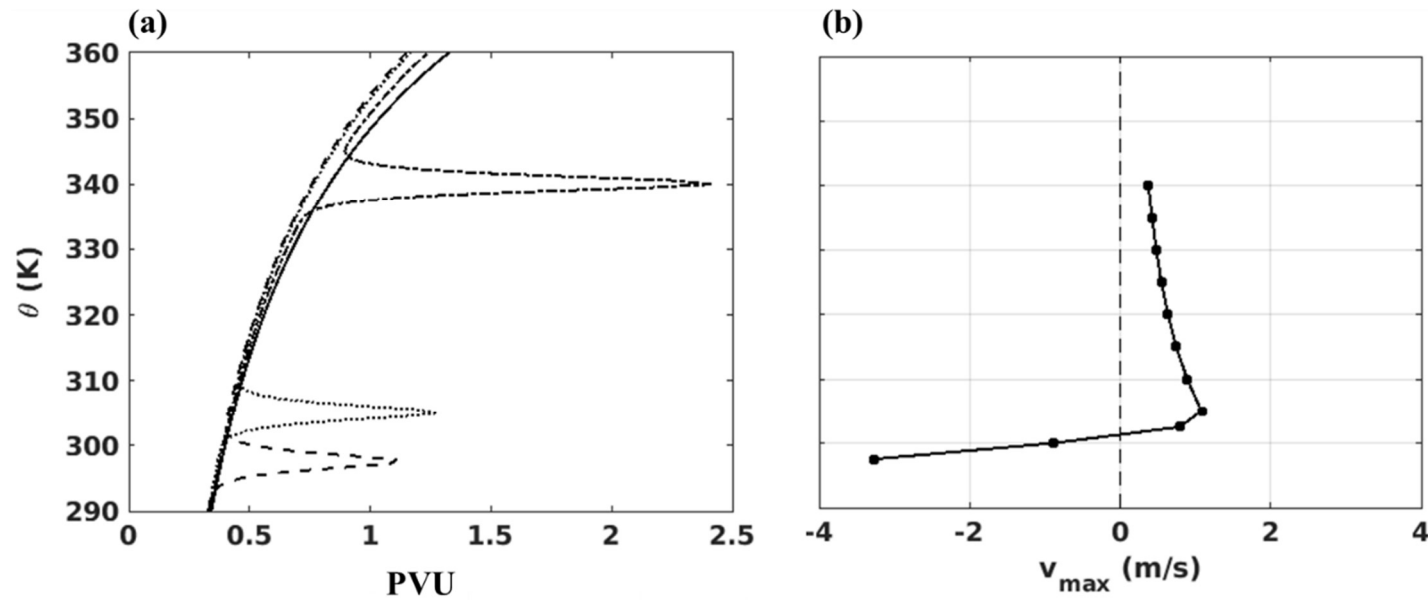
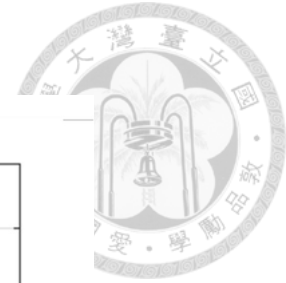


Figure 12. (a) Vertical profiles of PV for no inversion layer (solid line), low-level inversion (Dashed line), mid-level inversion (Dotted line), and high-level inversion (Dash-dot line). (b) the maximum wind speed change as a function of θ level where inversion layer located. Note that there is maximum wind speed when the inversion layer being at $\theta = 305$ K.

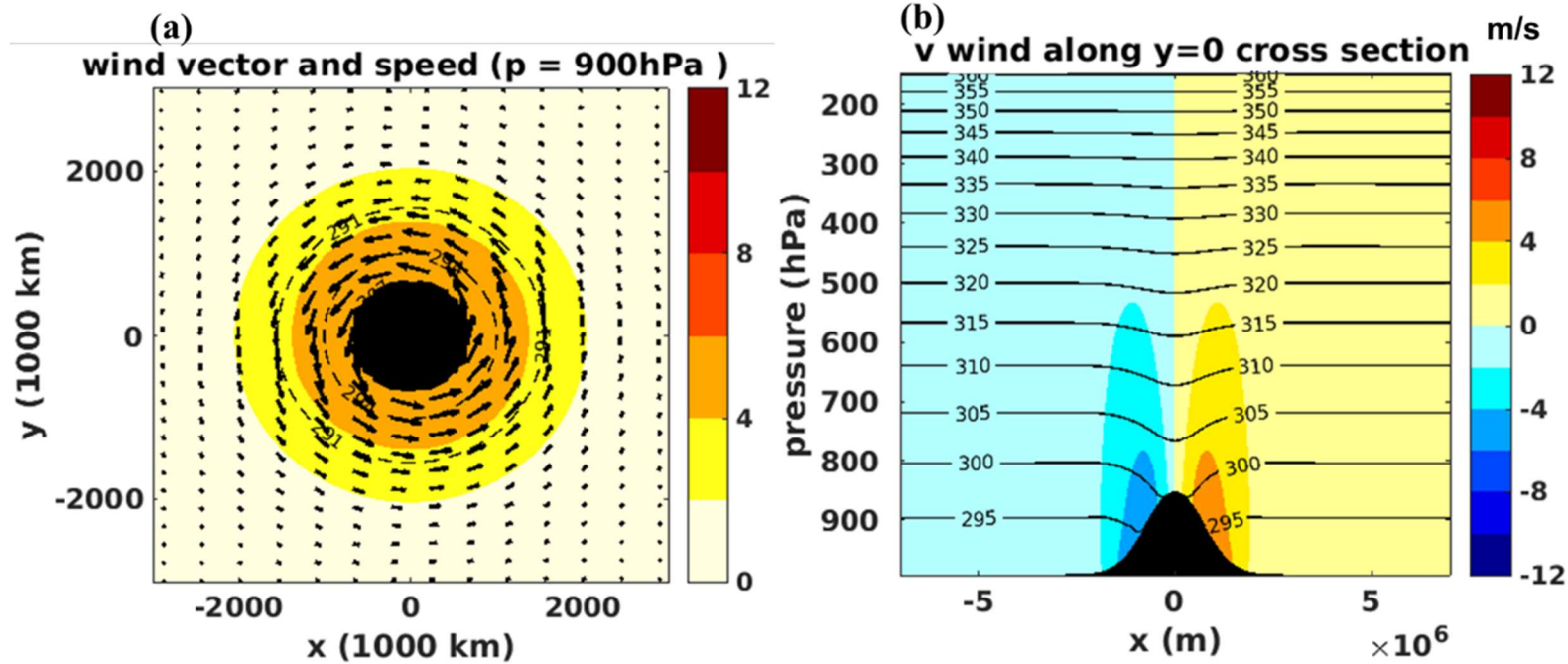


Figure 13. (a) Wind speed (shading), wind vector (quiver), and θ (contour) at 900hPa. (b) As in Figure 8(a), but we solved a 3-D invertibility problem. Both with circular surface thermal forcing $\theta_0 = 11$ K and orographic forcing $\Phi_0 = 1200$ km but with the governing equation being (41). The maximum wind is 5.7 m/s. Note that the magnitude of the LLJs is smaller than a 2D source case.

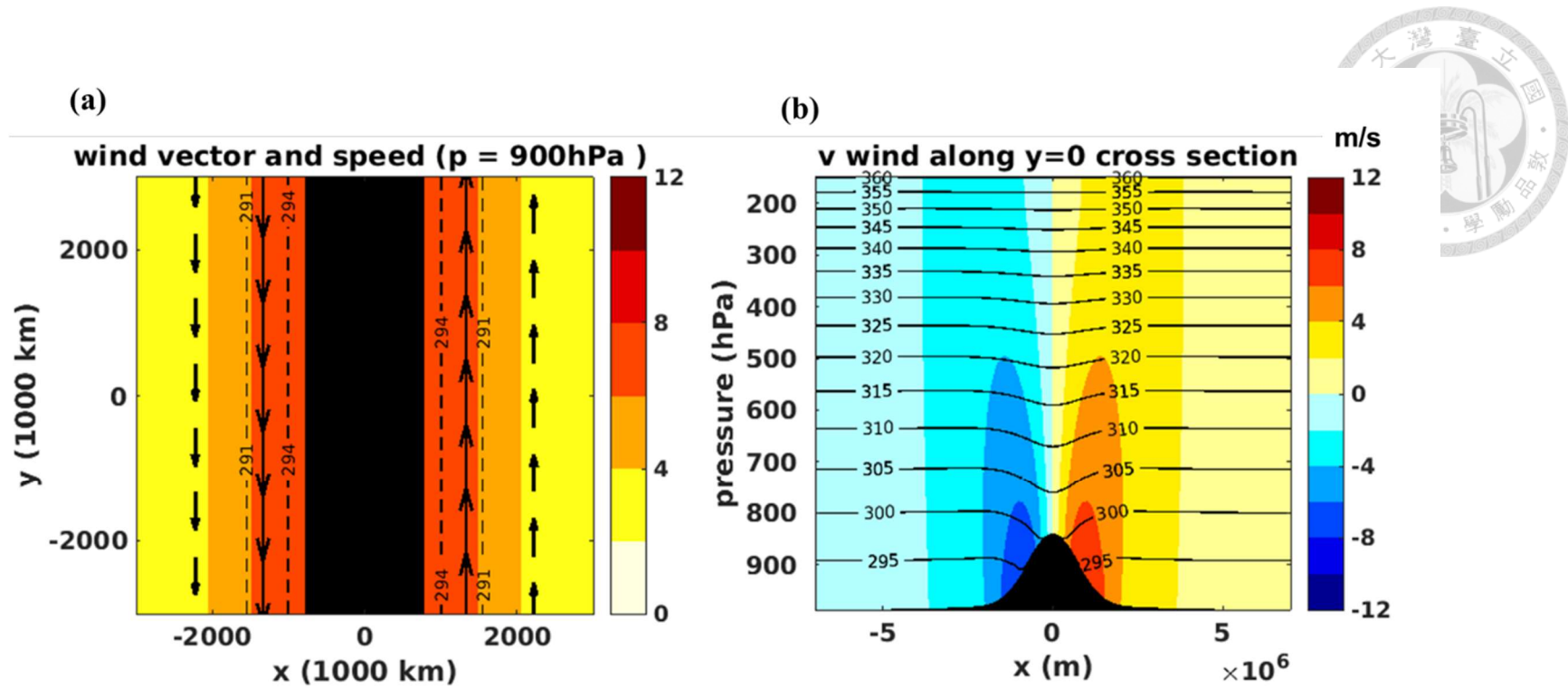


Figure 14. As in Figure 13, but with meridionally symmetric conditions. The maximum wind is m/s . Note that the magnitude of the LLJs significantly decreases compared to a 2-D source case.

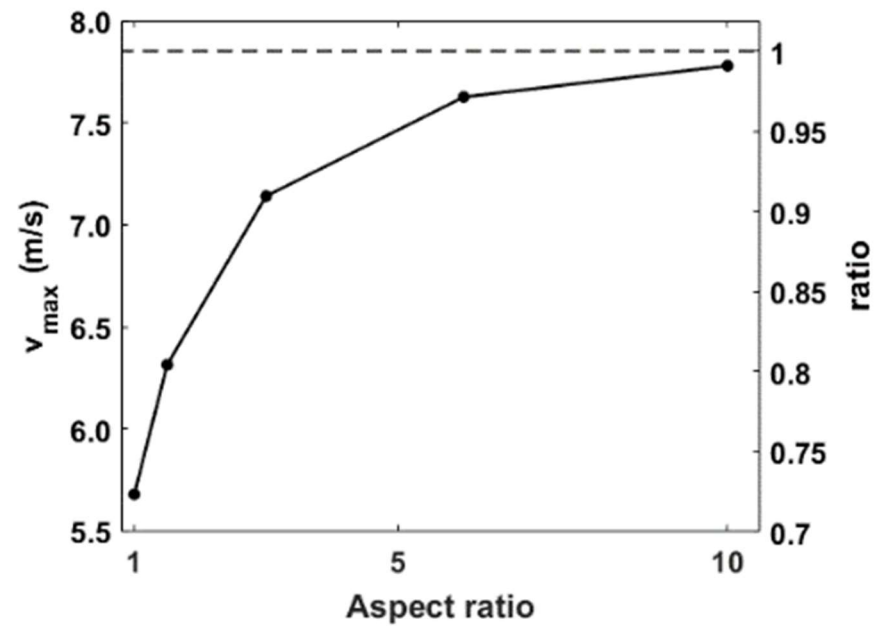


Figure 15. The maximum meridional wind for different aspect ratio. The dash line is a 2-D source case which the wind speed is maximized.

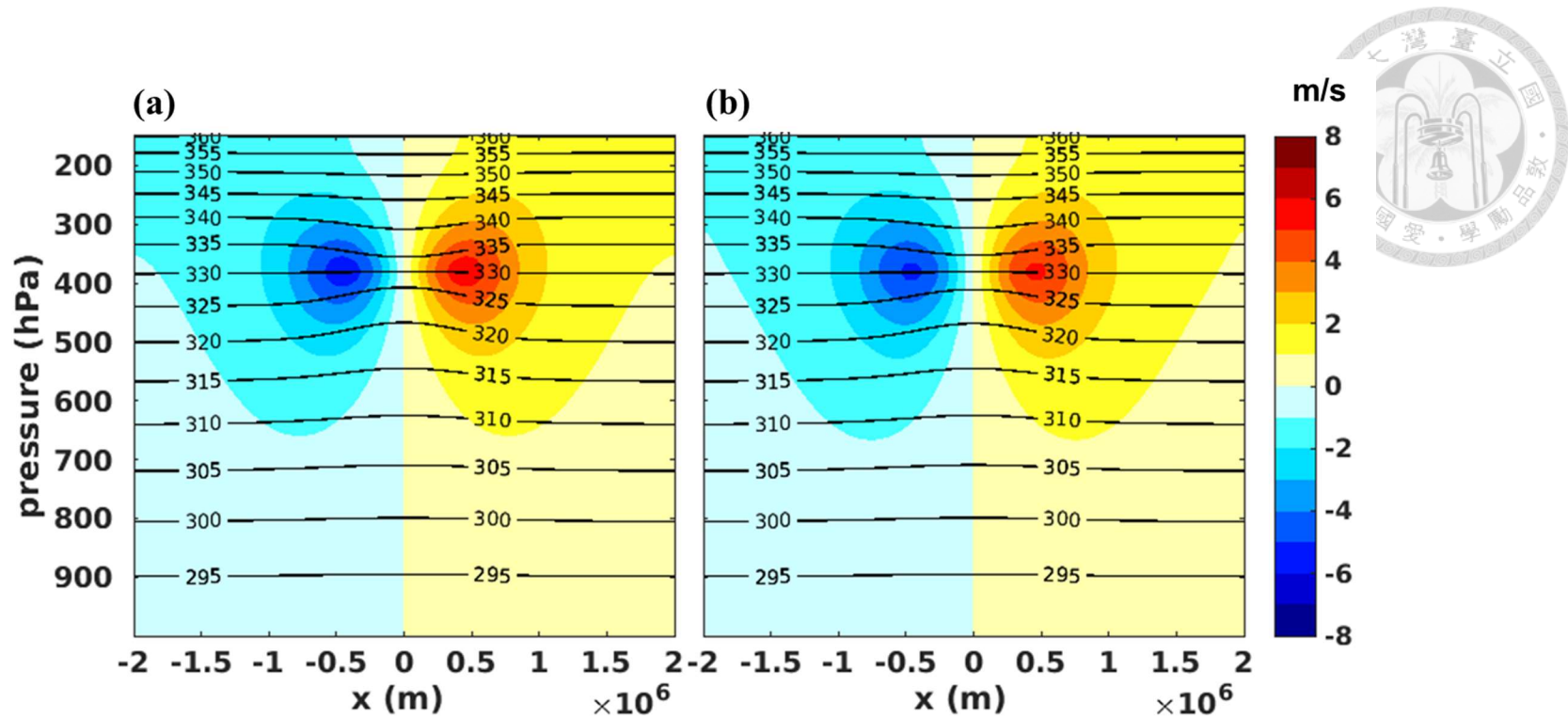


Figure 16. Numerical results for (a) linear balance (b) nonlinear balance relation in weak PV anomaly experiments, including induced cyclonic flow (shading, in m/s) and pressure (contour, in hPa). The maximum wind speeds are (a) 5.5 m/s (b) 5.1 m/s, respectively.

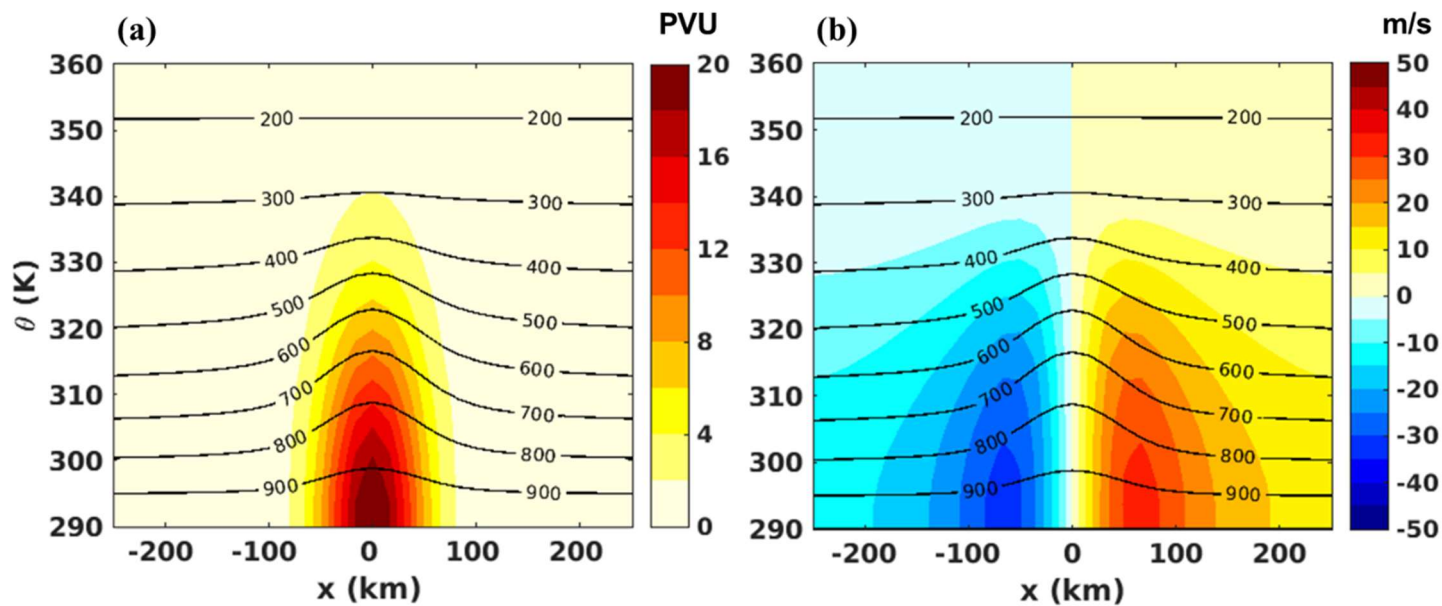


Figure 17. Numerical results for nonlinear balance relation invertibility. (a) A strong typhoon-like PV anomaly (shading, in PVU) (b) Induced cyclonic flow (Shading, in m/s) and pressure (contour, in hPa). The maximum wind speed is 32.1 m/s, which is located in about 70 km in radius and rapidly decays as height and radius increase.

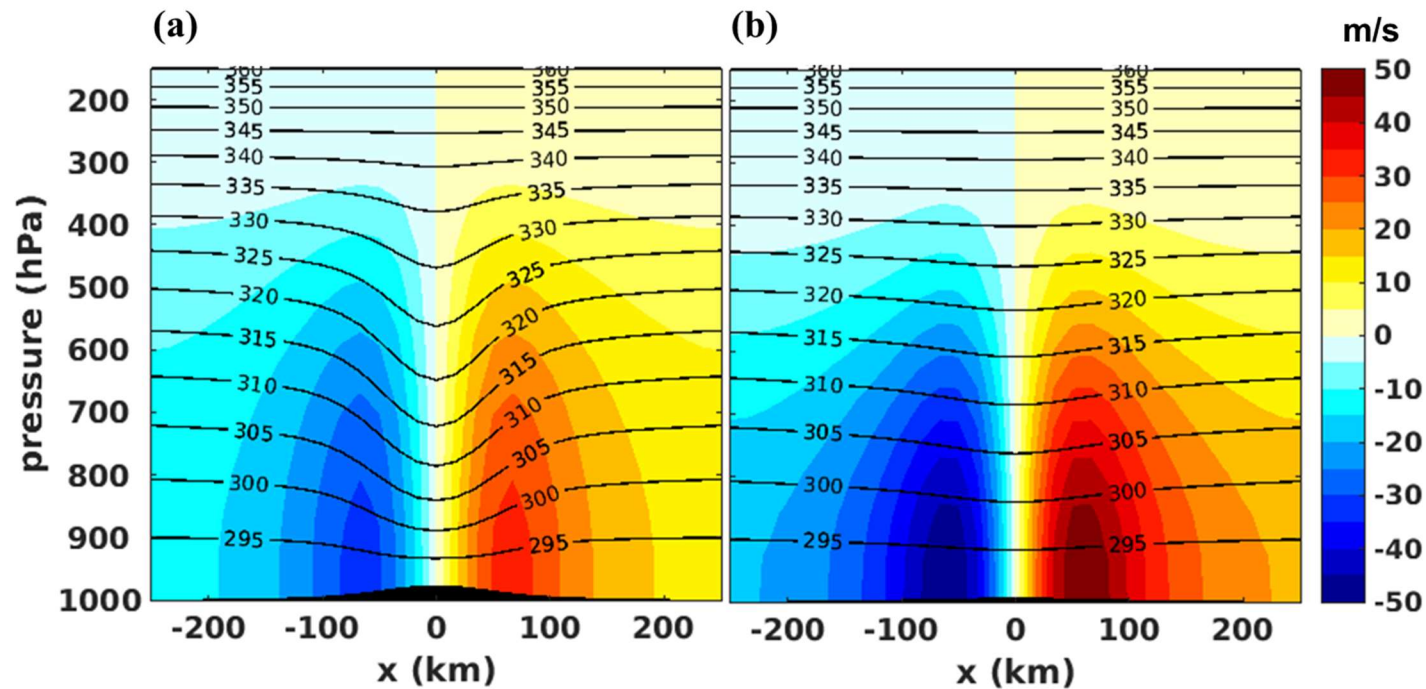


Figure 18. Numerical results for (a) linear balance (b) nonlinear balance relation in strong typhoon-like PV anomaly experiments, including induced cyclonic flow (shading, in m/s) and pressure (contour, in hPa). The maximum wind speed and minimum pressure are (a) 49.0 m/s and 995 hPa (b) 32.1 m/s and 976 hPa, respectively. Both of their maximum wind speeds are located in about 70 km. Note that significant center warming and pressure fall occur only when gradient wind balance is applied.

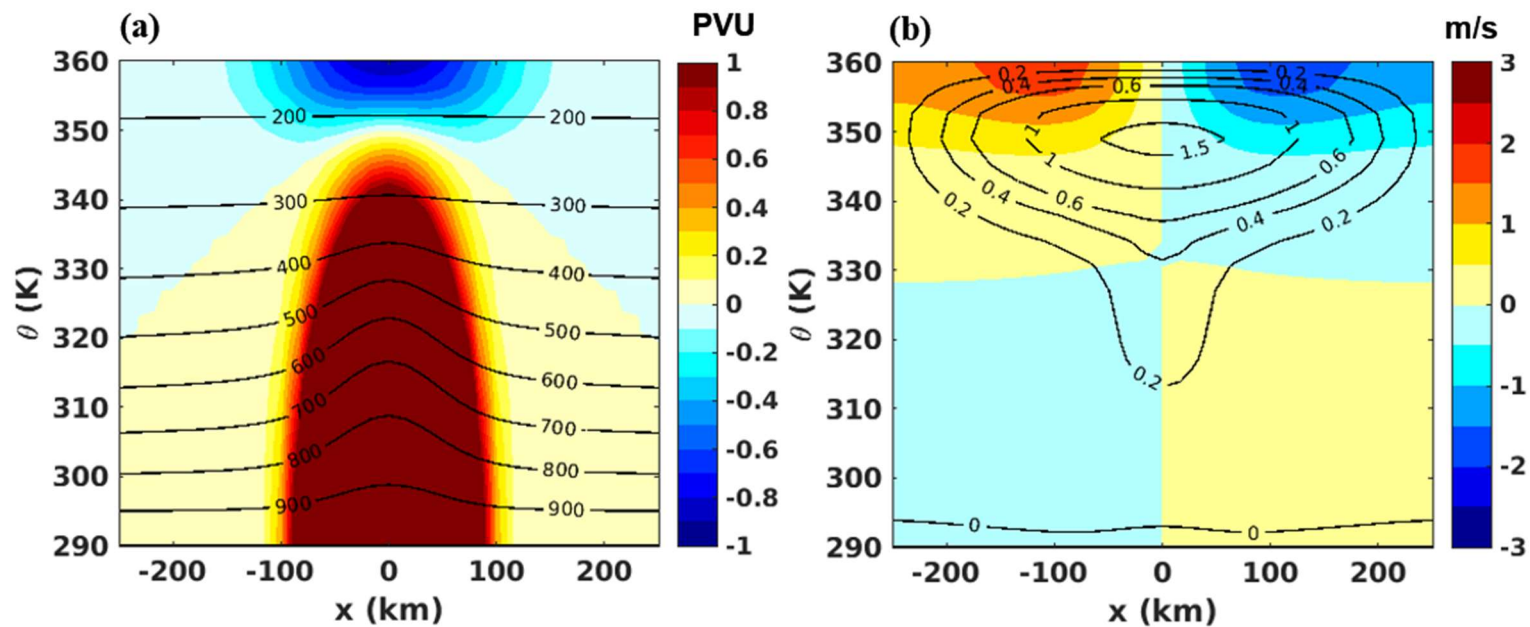


Figure 19. The invertibility problem with extra upper negative PV anomaly. (a) PV anomaly (shading, in PVU) (b) Wind and pressure difference with Figure 18 are presented in shading and contour, respectively. Note that the maximum pressure difference appears right below negative PV anomaly and decays as the height decrease.

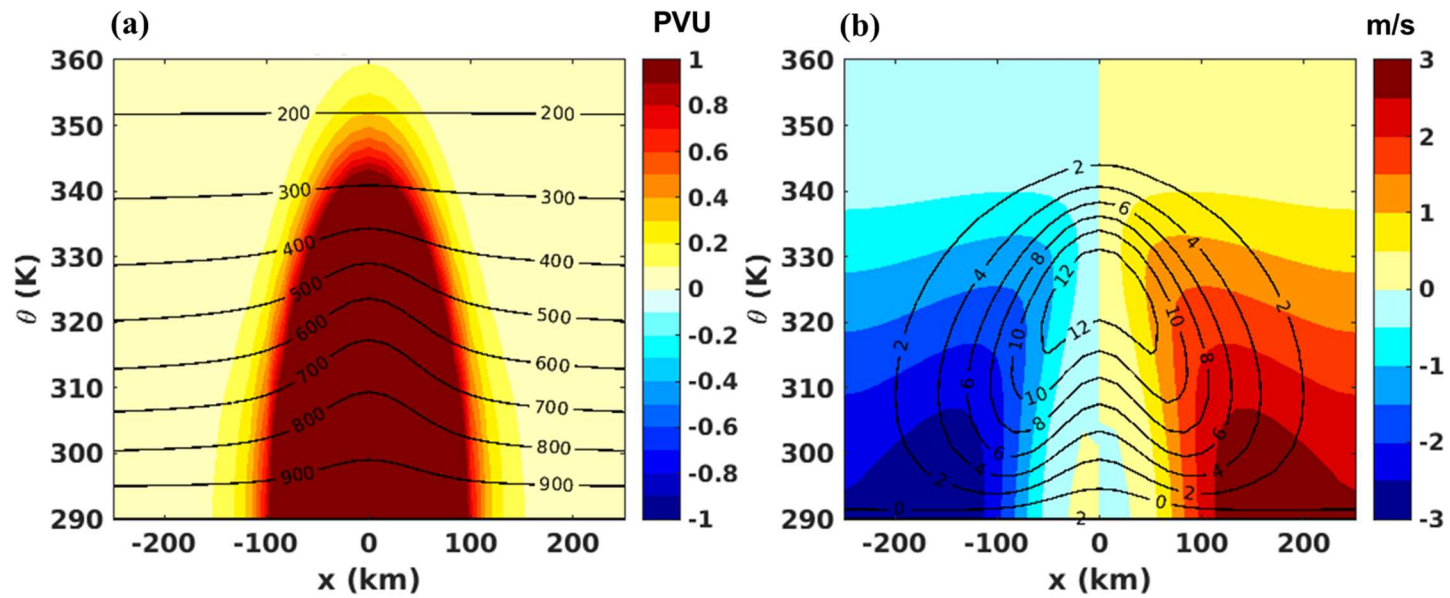


Figure 20. As in Figure 19, but with meridionally symmetric conditions. Note that the maximum pressure difference appears right above the positive PV anomaly and spreads more in vertical direction than in Figure 19.

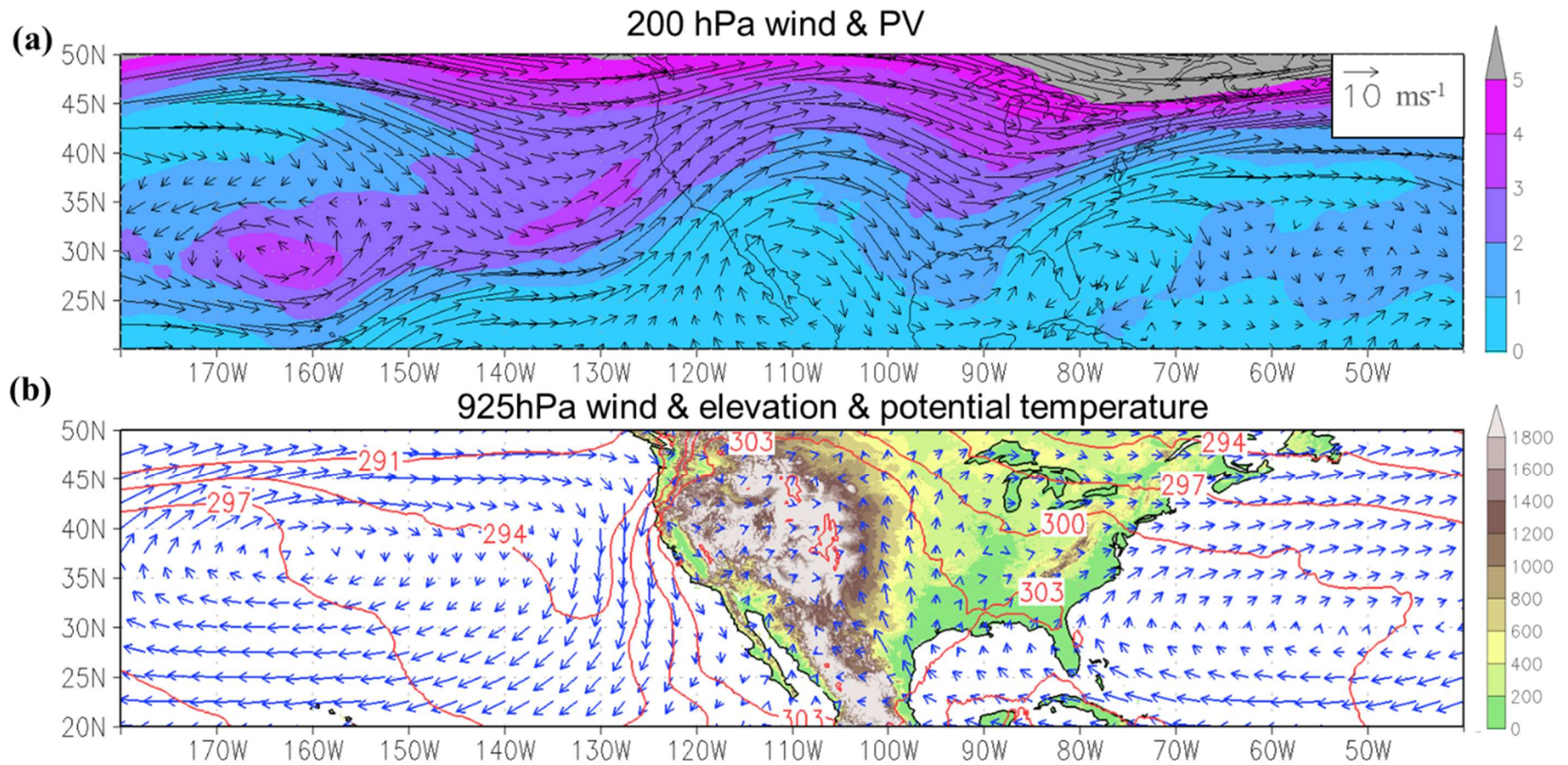


Figure 21. (a) Mean wind (quiver, in m/s) averaged over July, 2020 from ERA5 reanalysis data at (a) 200hPa (b) 925hPa level. The shading is (a) PV field (in PVU) and (b) elevation (shading, in meter). The contour in (b) is potential temperature.

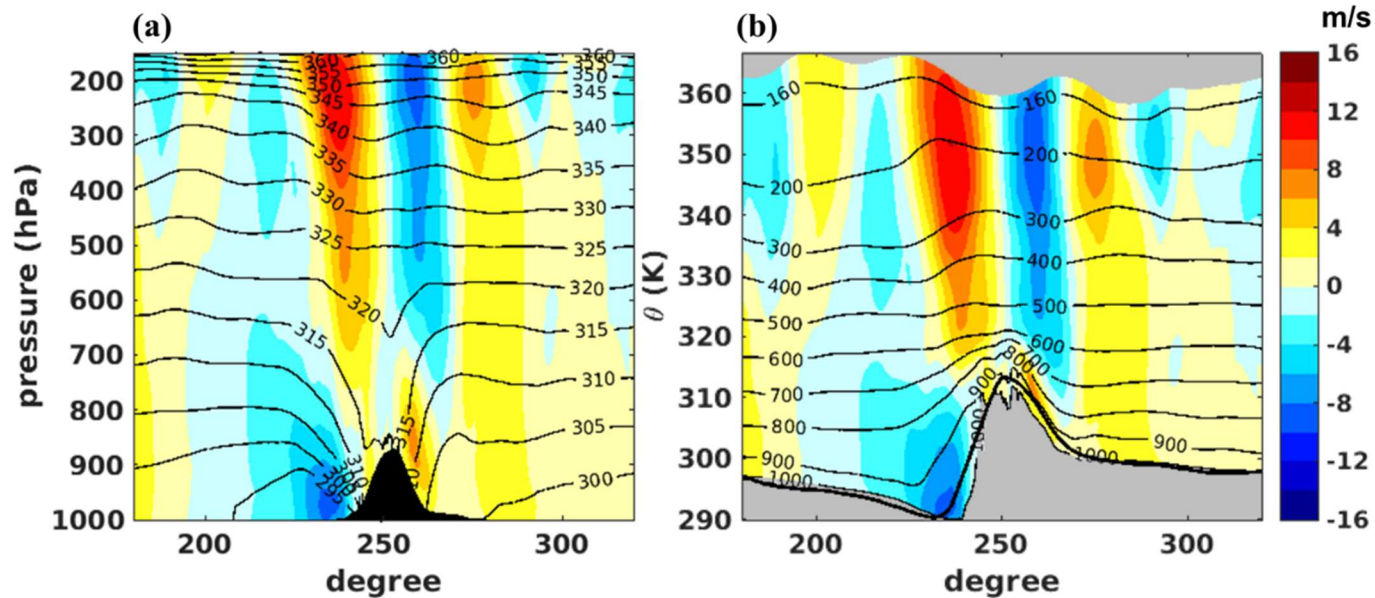


Figure 22. (a) Mean cross sections of meridional wind (shading, in m/s) averaged over the latitude sector 30-35°N from ERA5 reanalysis data and (b) interpolation to longitude-potential temperature cross sections from (a). Contour is (a) isentropes (in K) (b) isobars (in hPa). Black region is topography and gray shading is the domain out of the physical region. Here we choose $p = [1000, 150]$ hPa. We can identify cyclonic LLJs patterns near The Rocky Mountains.

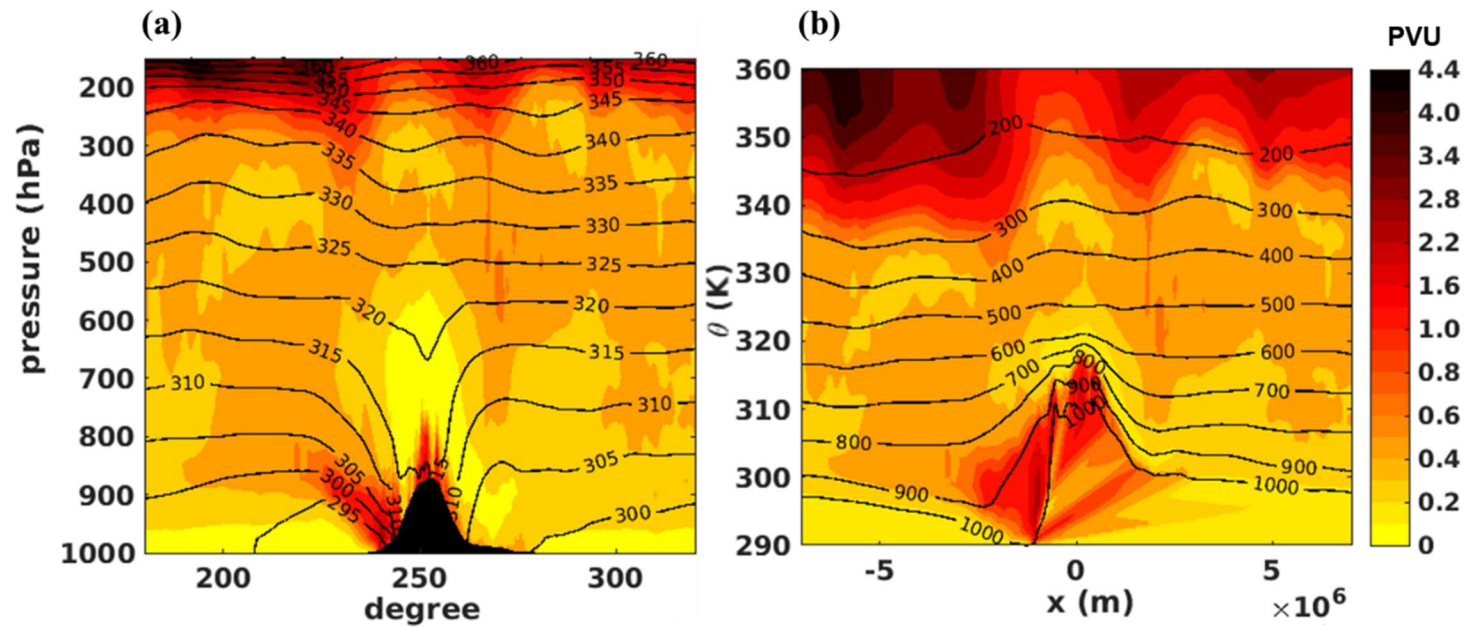


Figure 23. (a) Mean cross sections of PV (shading, in PVU) averaged over the latitude sector 30-35° N from ERA5 reanalysis data and (b) interpolation to longitude-potential temperature cross sections from (a). Contour is (a) isentropes (in K) (b) isobars (in hPa). Black region is topography.

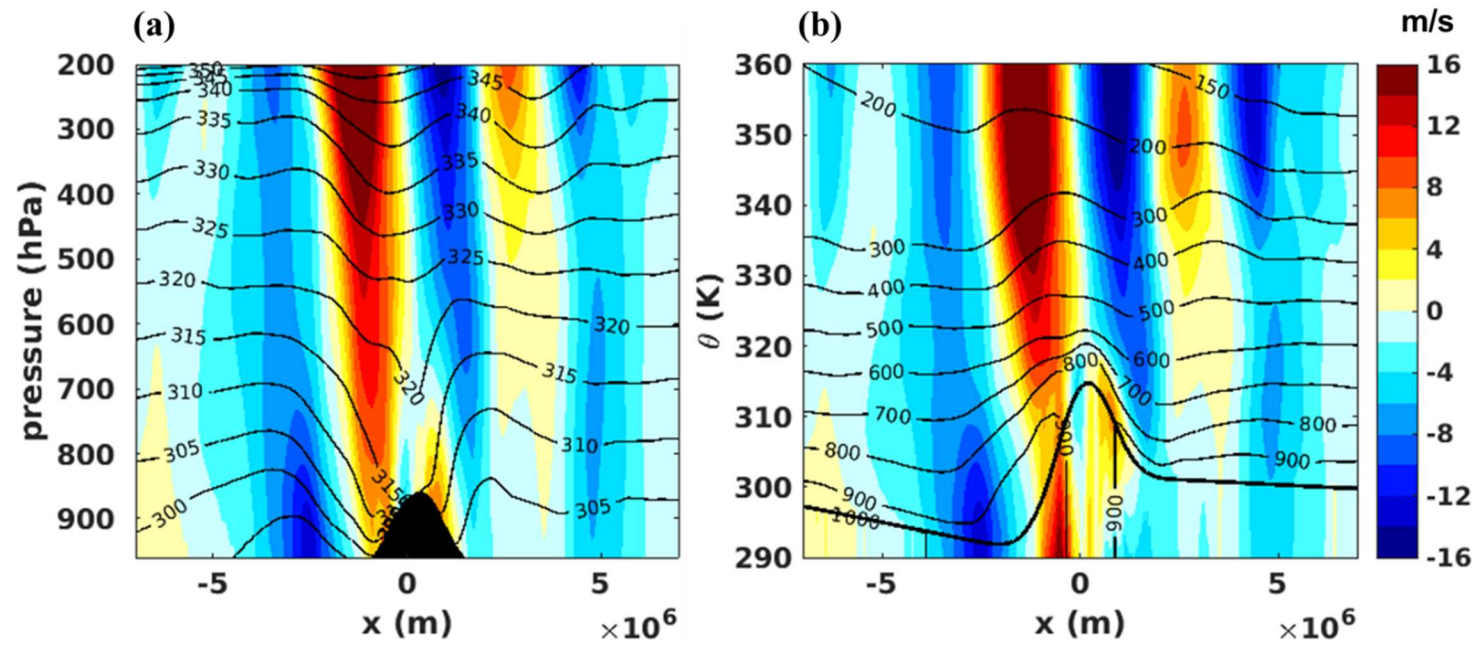


Figure 24. Meridional wind field (shading) in (a) isobaric coordinate with θ (contour) and (b) isentropic coordinate with pressure (contour). Black region in (a) is topography and we choose the domain out of $p=(1000\sim 150$ hPa). The patterns of wind field are similar with observations (Figure 22).

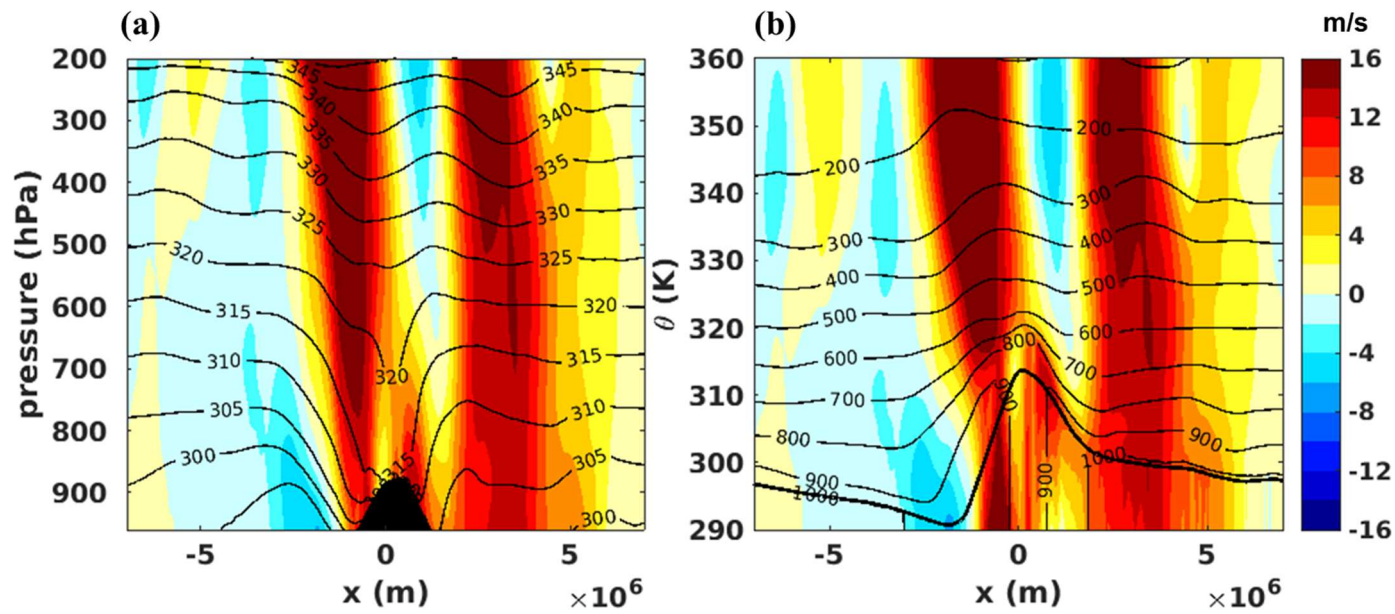


Figure 25. As in Figure 24, but with θ_s and the top pressure assigned by interpolation. The patterns of wind field are similar to observations (Figure 22), but too large southerly at the east of The Rocky Mountains.

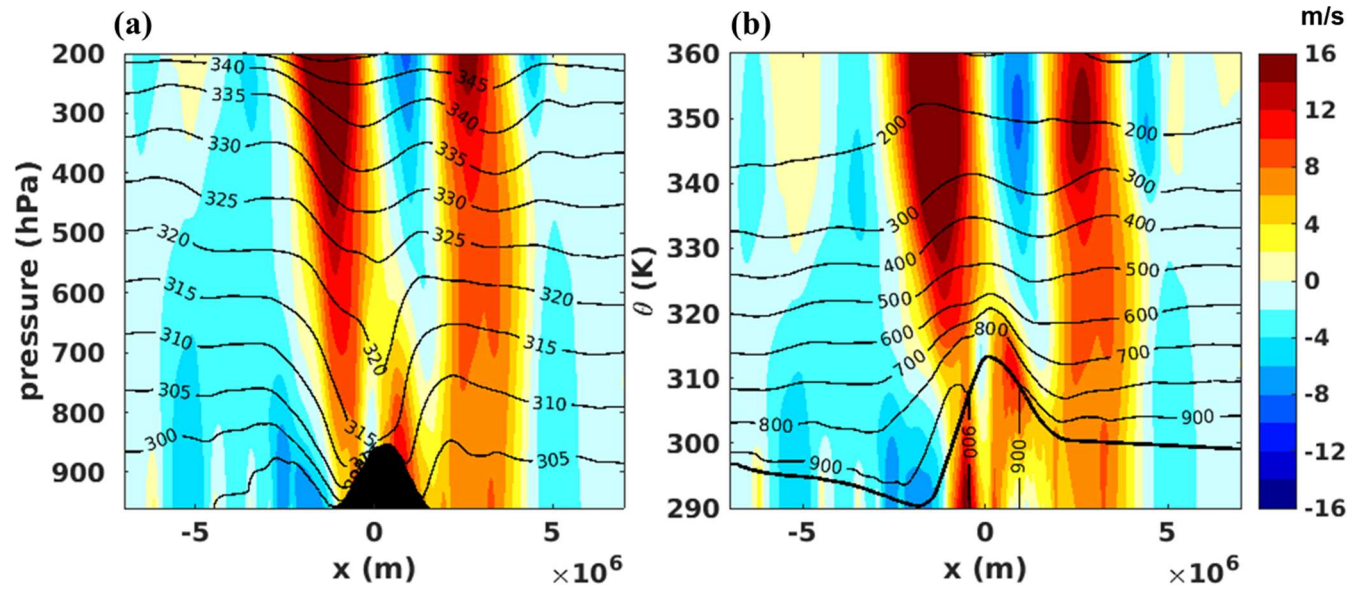


Figure 26. As in Figure 25, but with smaller θ_S slope at the east of the mountain. The wind field is more like observations (Figure 22).

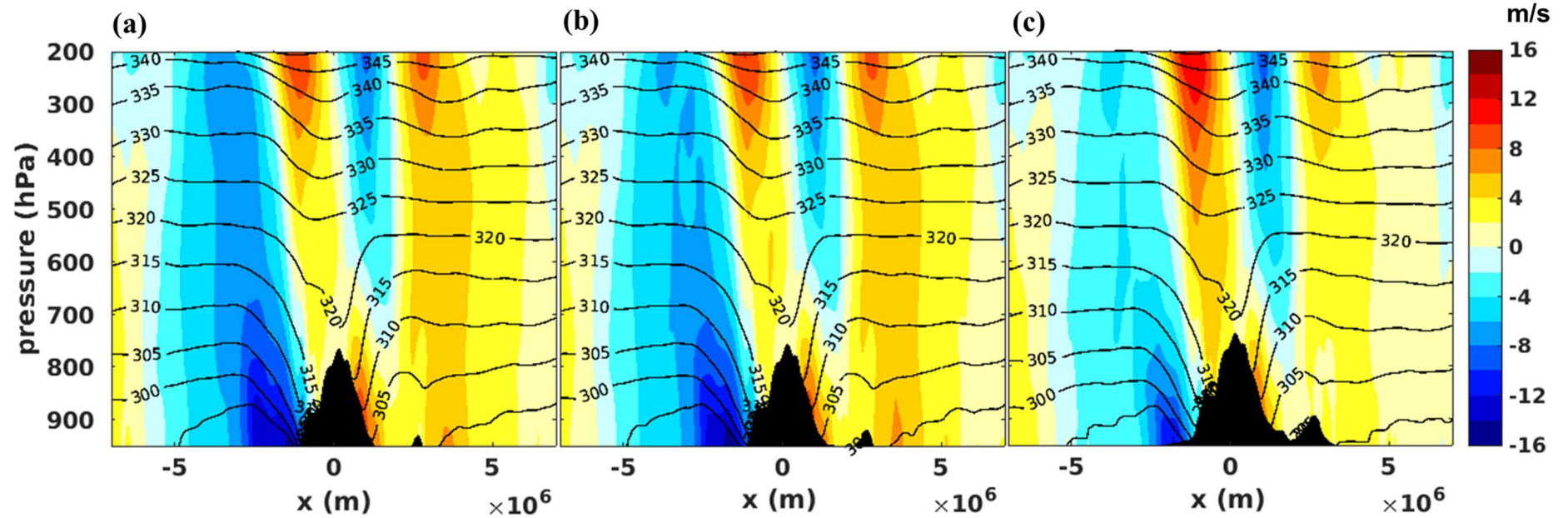


Figure 27. The cross section of meridional winds (shading, in m/s) and θ (contour, in K) at 35°N for the 3-D balanced model results. Lift massless layer temperature for (a) 0hPa (b) 25 hPa (c) 50 hPa. The black region is topography. Their northerly wind speed at the west of the mountain is up to (a) 18 m/s (b) 16 m/s (c) 12 m/s.

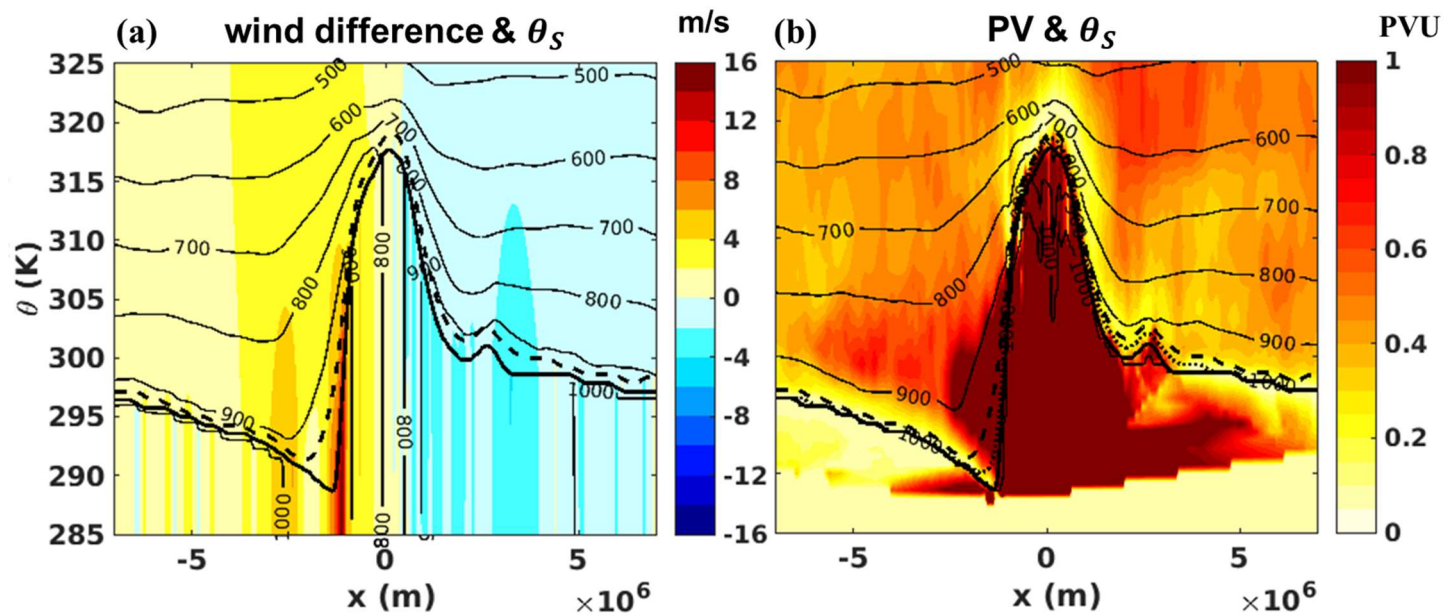


Figure 28. (a) The wind difference (shading, in m/s) between lifting massless layer for 50 hPa and 0 hPa and (b) the PV field (shading, in PVU). Thin contours are interpolated pressure. Depicting domains are between $\theta = 295$ K and $\theta = 325$ K. Solid, dotted, and dash lines are for no lifting, 25 hPa lifting, and 50 hPa lifting, respectively.

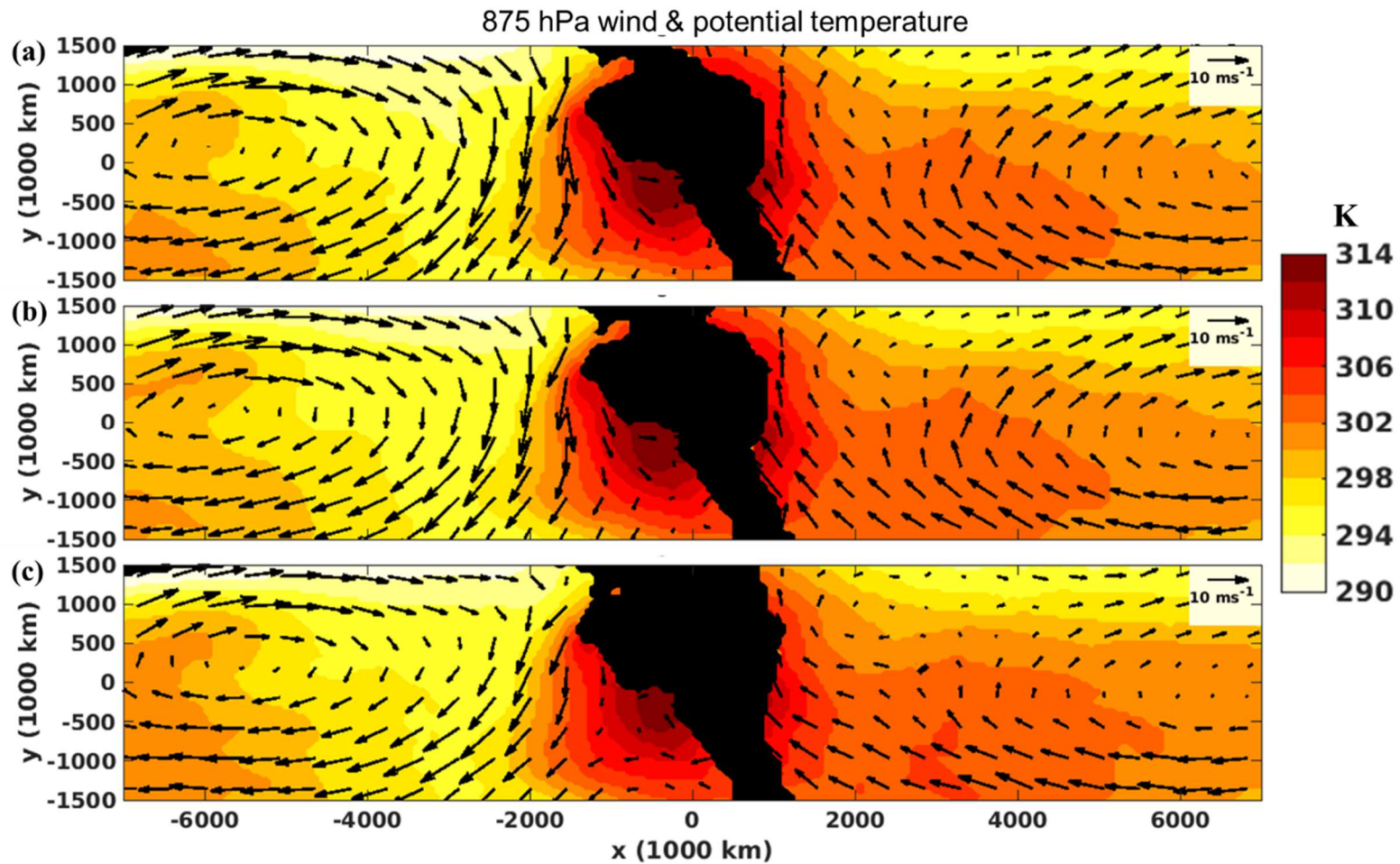


Figure 29. The horizontal wind fields (quiver, in m/s) and θ fields (shading, in K) at 875 hPa for the 3-D balanced model results near the Rocky Mountains. Lifting massless layer temperature for (a) 0hPa (b) 25 hPa (c) 50 hPa. The black region is topography.

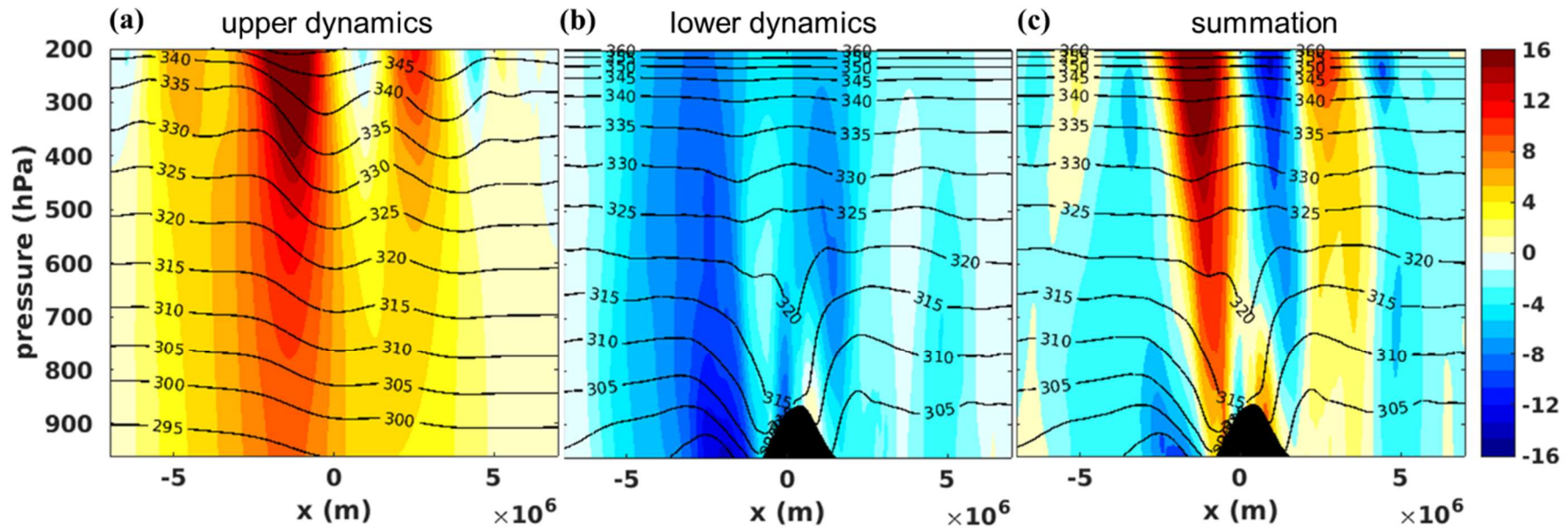


Figure 30. Meridional wind fields (shading, in m/s) in isobaric coordinate with θ (contour, in K). (a) Upper dynamics case. The PV field value below 330 K is zonally averaged and the topography and surface thermal forcing is set to be zero. (b) Lower dynamics case. The PV field value above 330 K is zonally averaged. (c) the summation of upper dynamics and lower dynamics wind field. Note that in convenience we directly applied the pressure contour of lower dynamics in (c).

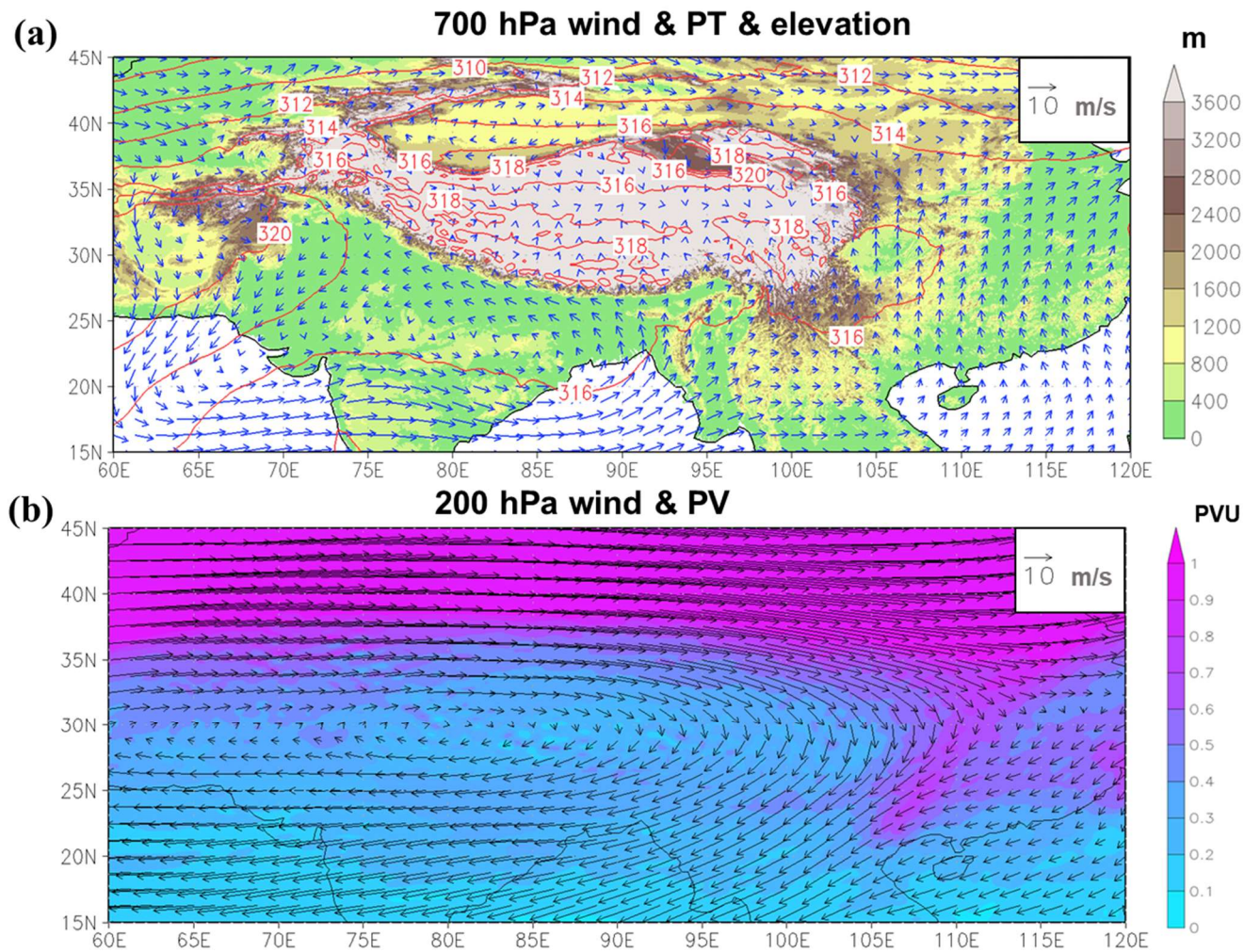


Figure 31. (a) Mean wind field (quiver, in m/s), potential temperature at 700 hPa, and elevation (shading, in meter). (b) Wind field (quiver, in m/s) and PV (shading, in PVU) at 200 hPa. All fields are averaged over July, 2020 from ERA5 reanalysis data.

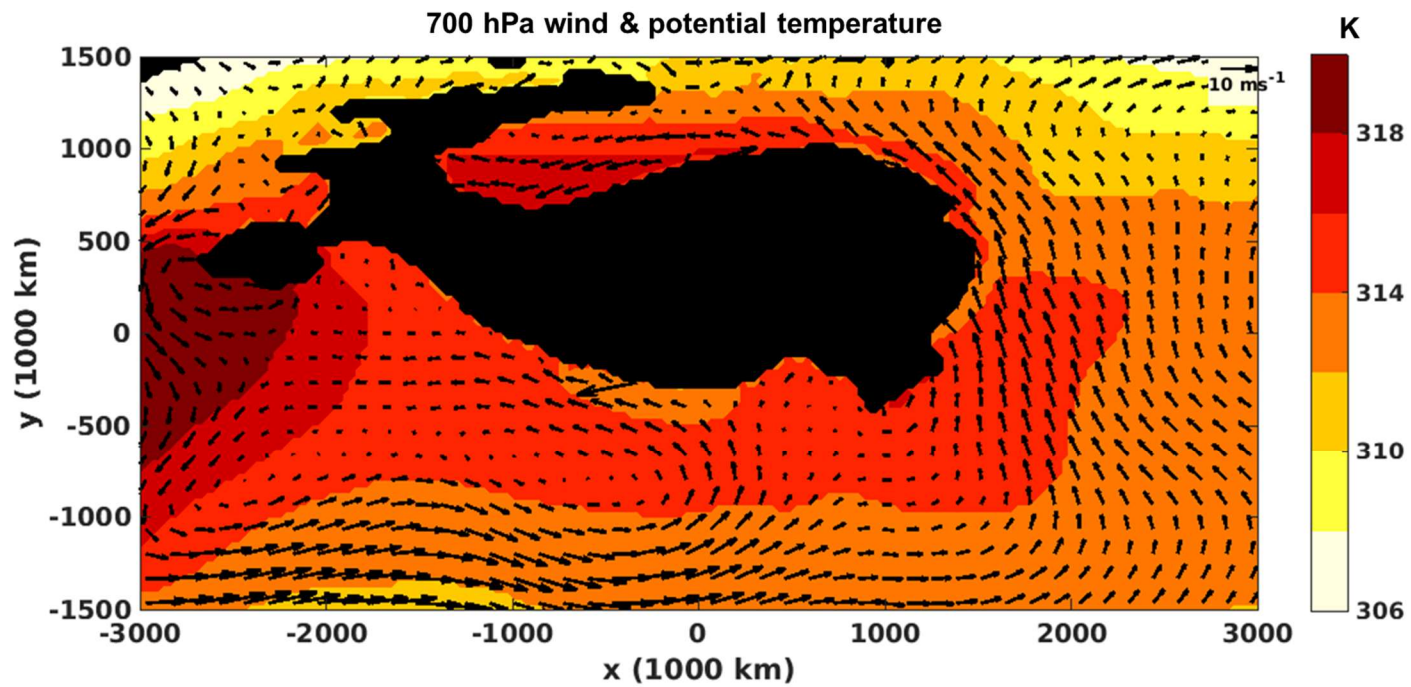


Figure 32. Mean wind field (quiver, in m/s) and potential temperature (shading, in K) at 700 hPa. Lifting massless layer temperature for 50 hPa is used in this result.

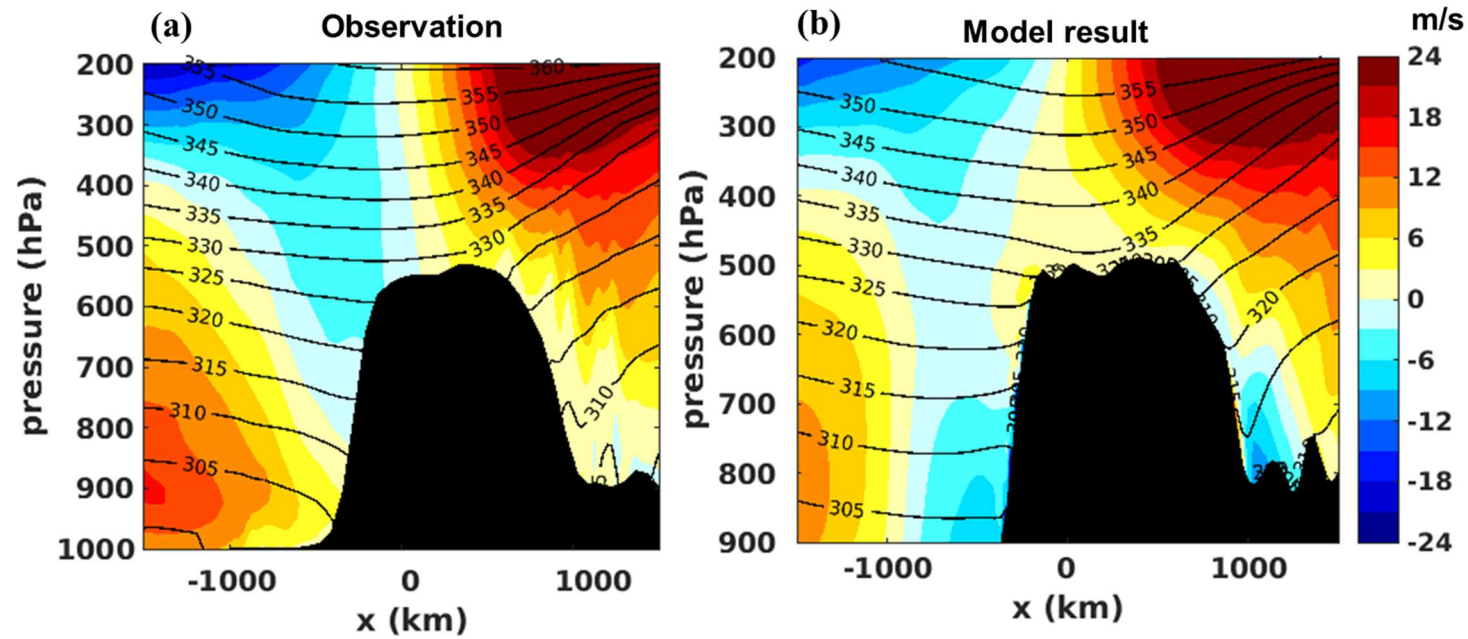


Figure 33. (a) Observation (b) numerical result for the cross section of u wind (shading, in m/s) and potential temperature (contour, in K) at 90°E.

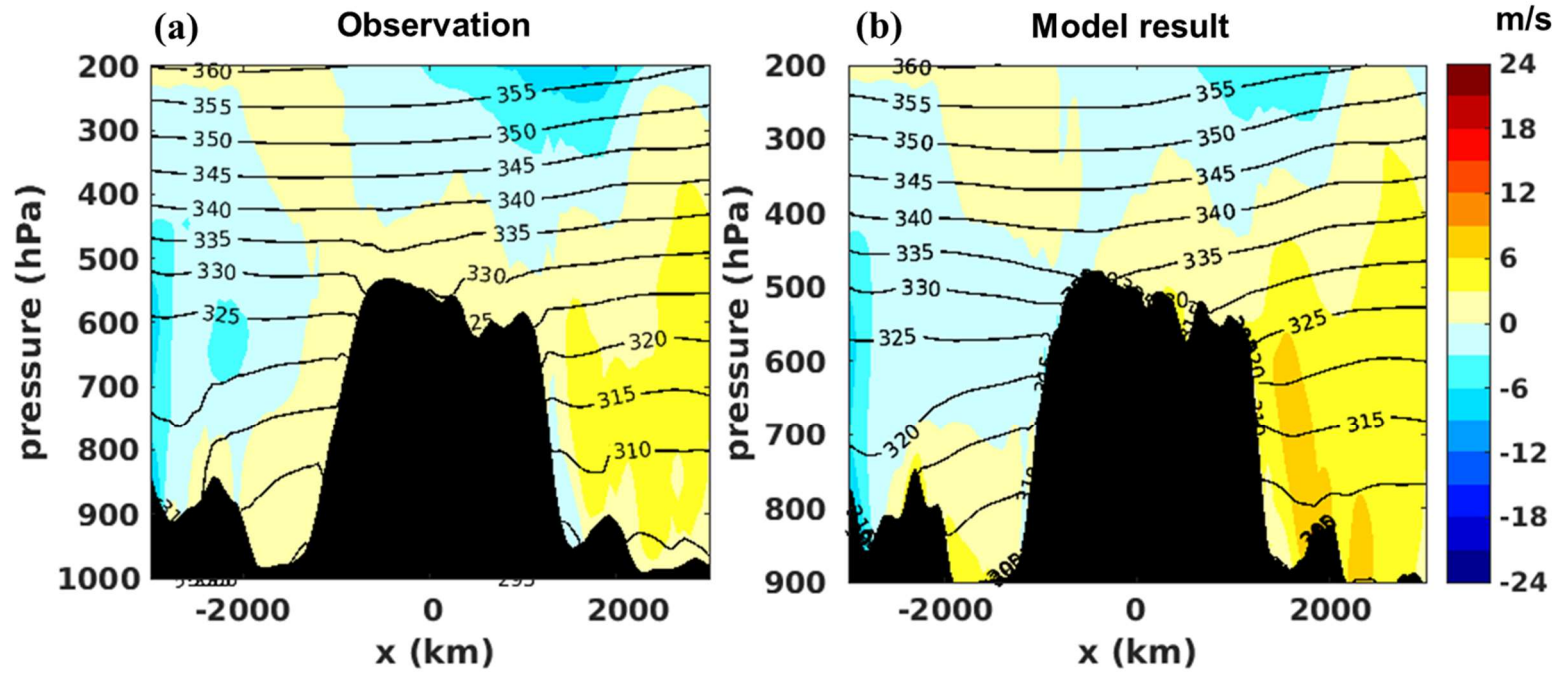


Figure 34. (a) Observation (b) numerical result for the cross section of u wind (shading, in m/s^{-1}) and potential temperature (contour, in K) at 30°N.

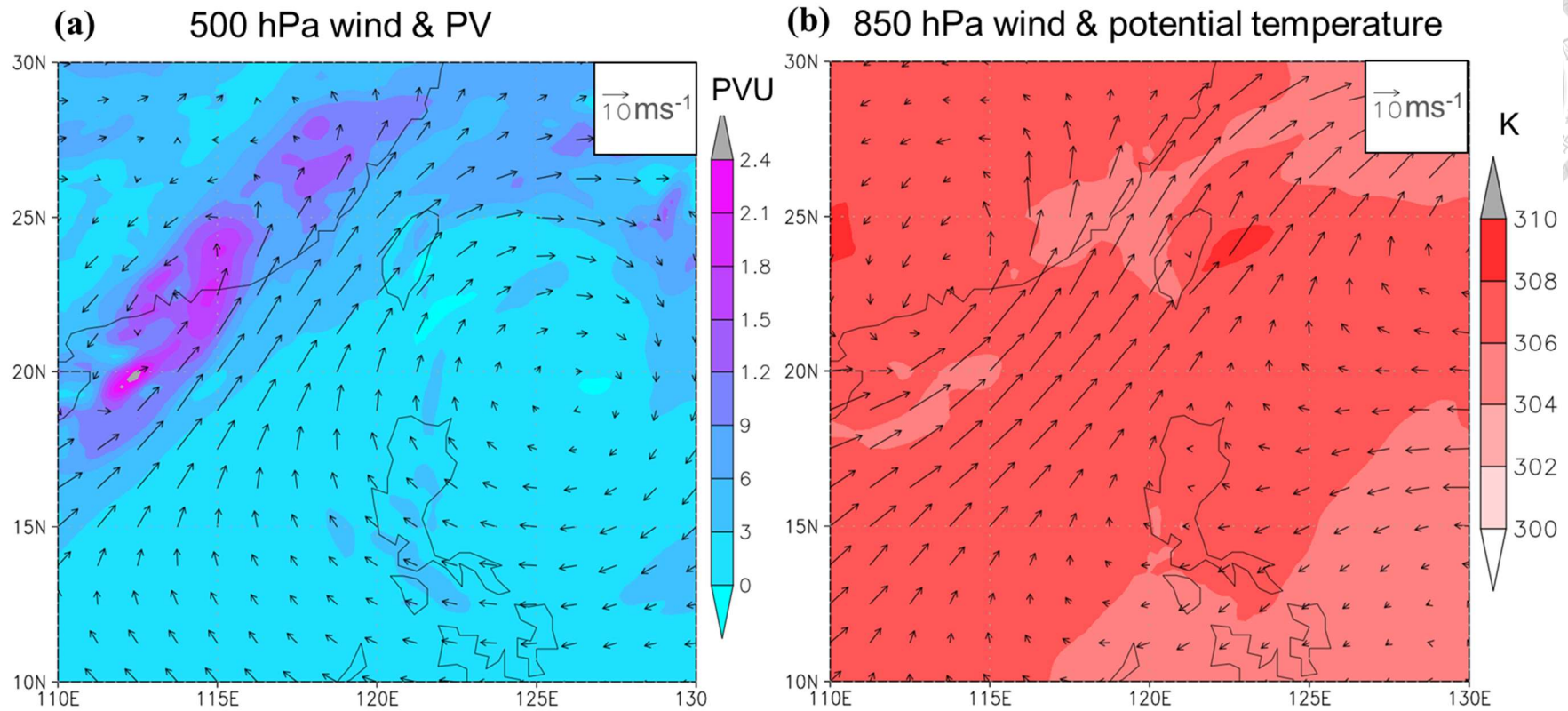


Figure 35. (a) Mean wind field (quiver, in m/s) and PV field (shading, in PVU) at 500 hPa. (b) Wind field (quiver, in m/s) and temperature (shading, in K) at 850 hPa near Taiwan. All fields are averaged from 0000 UTC to 2400 UTC on 20 July 2015 from ERA5 hourly reanalysis data.

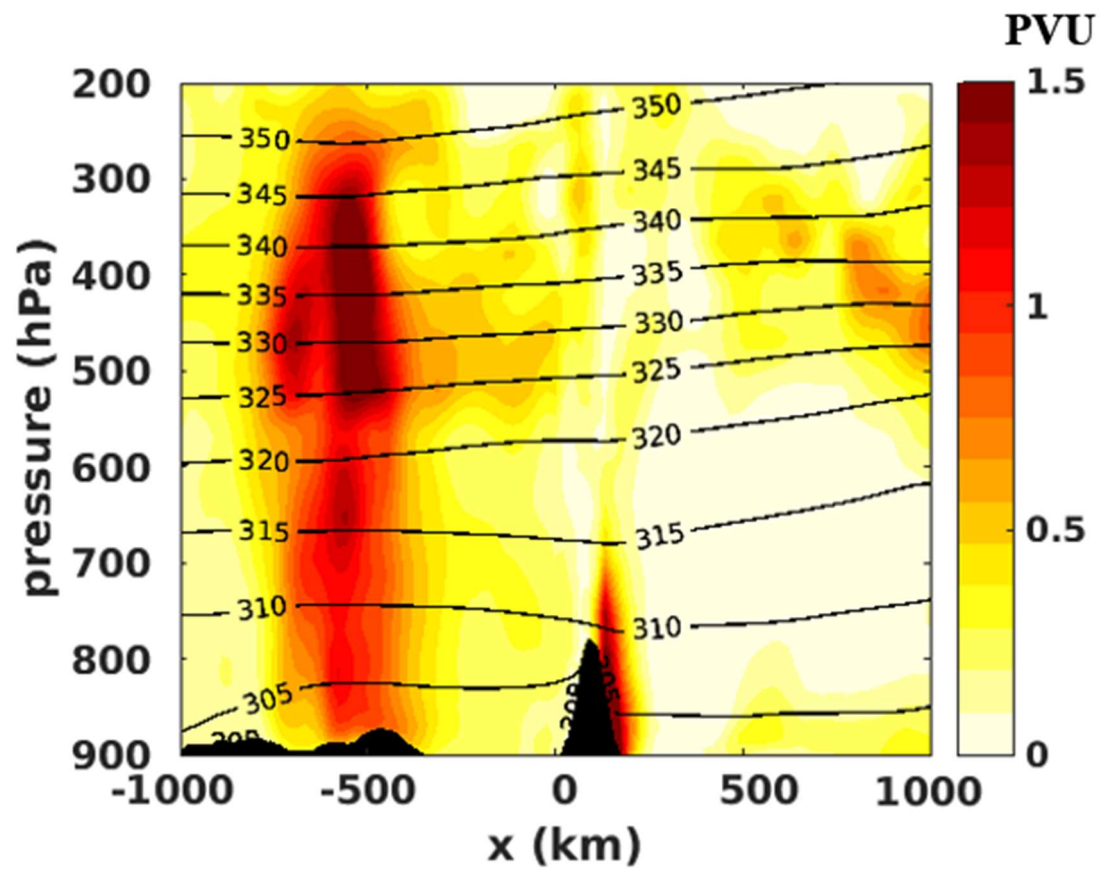


Figure 36. Cross sections of PV (shading, in PVU) and potential temperature (contour, in K) at 23°N from ERA5 reanalysis data. This cross section contains the Taiwan island.

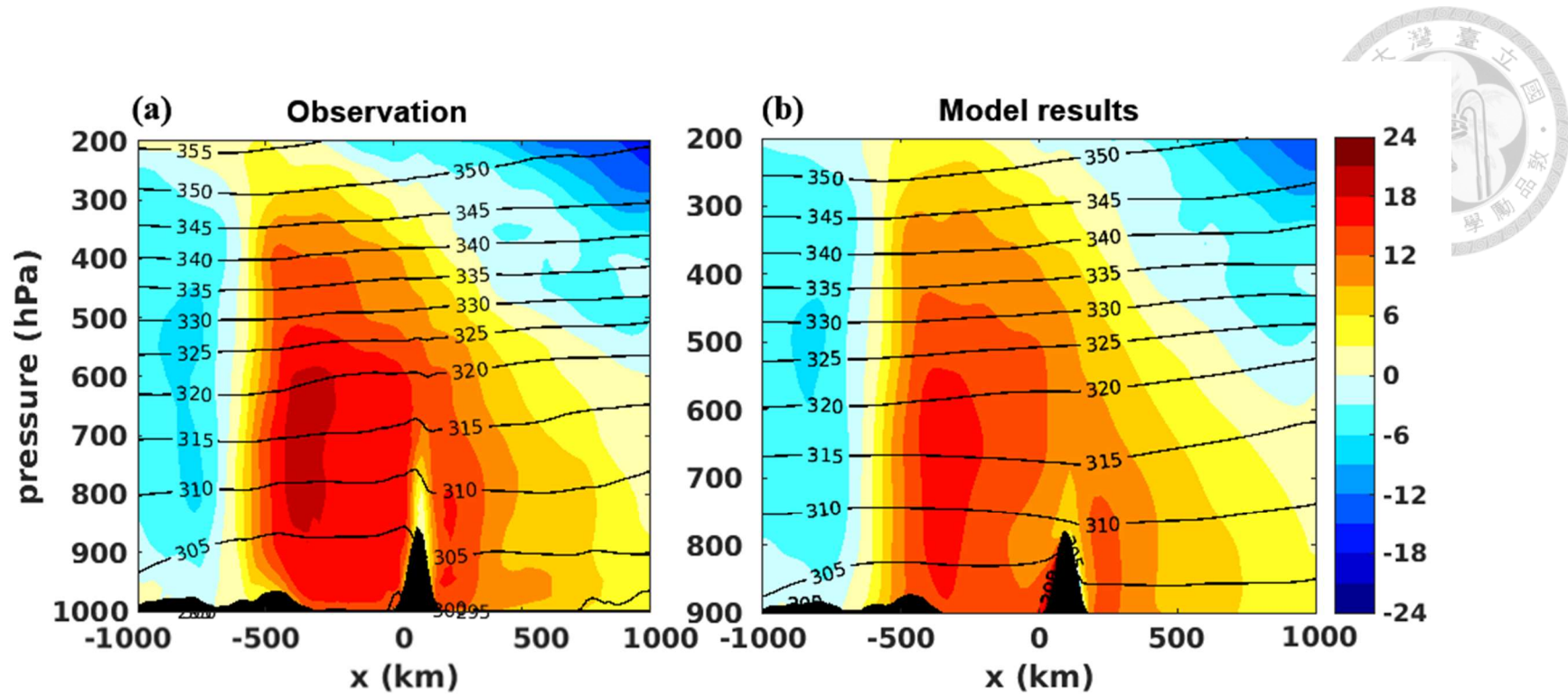


Figure 37. (a) Observed fields (b) numerical results for cross sections of v wind (shading, in m/s) and potential temperature (contour, in K) for 23°N near Taiwan. Note that massless layer temperature θ_s are lifting for 50 hPa. The maximum southerly is about (a) 19.2 m/s (b) 16.5 m/s

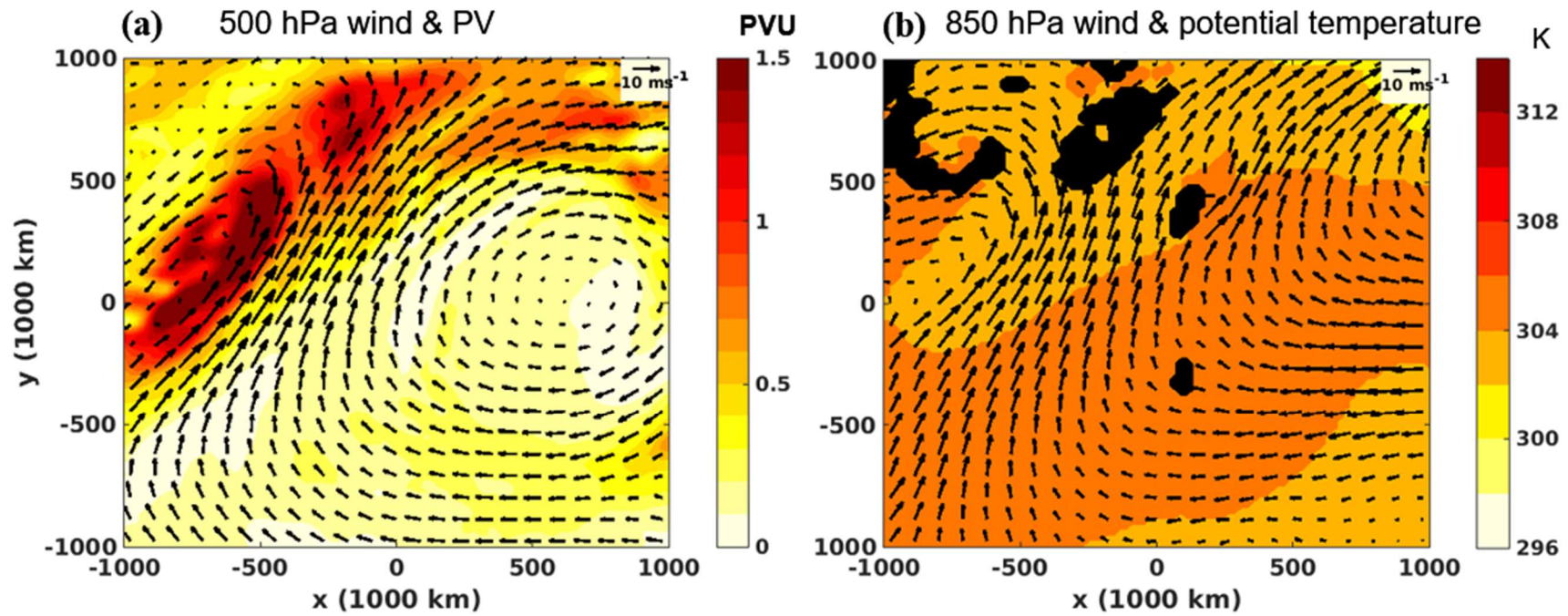


Figure 38. (a) Mean wind field (quiver, in m/s) and PV field (shading, in PVU) at 500 hPa. (b) Wind field (quiver, in m/s) and temperature (shading, in Kelvin) at 850 hPa near Taiwan. The position of the Taiwan island is at about $(x, y) = (100, 300)$ km. Note that massless layer temperature θ_s are lifting for 50 hPa.